Infrared Spectroscopy Of Ba_{3+y} $Co_{1+x}Nb_2O_9$ Ceramics

by

Samia Ibrahim

A THESIS SUBMITTED IN PARTIAL FULFILMENT OF
THE REQUIREMENTS FOR THE DEGREE OF

MASTER OF SCIENCE

in

The Faculty of Mathematics and Sciences

Department of Physics

BROCK UNIVERSITY

September 12, 2017

Abstract

The dielectric properties of ceramic Ba_{3+y} $Co_{1+x}Nb_2O_9$ where x= 0,-0.07,0.03 and y = 0, -0.03 were characterized because it might used for a wide range of applications including wireless communication used in mobile communication, ultra high speed local area networks, intelligent transport system and satellite communications.

Room temperature optical reflectivity measurements of ceramics sintered at different temperatures between 1200 °C to 1500 °C were made covering the spectral range between 70-8000 cm^{-1}. The Lorentz model was used to fit the reflectance data to make extrapolations for Kramers Kronig (K-K) analysis and to estimate the microwave properties.

K -K analysis was applied to extract the other optical response functions from the reflectance data (optical conductivity and dielectric permittivity).

Powder X-Ray diffraction measurements were done with 2θ in the range between 10 to 80 degree for all samples. Most samples exhibit some degree of 1:2 ordering which appears as small superlattice peaks at 17.6 and 12 degree. All samples exhibit a small amount of impurity phases.

The main purpose of this work is to study the effect of the density, 1:2 (Co:Nb) ordering and concentration of Cobalt on the dielectric properties. It was shown that density has a clear effect on the dielectric properties. For example ϵ_1 (50 cm^{-1}) decreased if the density decreased. On the other hand the change of the concentration of Cobalt does not have any real effect on the dielectric properties. 1:2 order also has an effect on the dielectric properties. It was observed that the scattering rate of the optical phonon was smaller in sample exhibiting more 1:2 order.

Contents

List of Figures

List of Tables

Chapter 1

Introduction

During recent decades, much research has been done to find high quality and low cost materials for microwave communications. Ceramic perovskite-related ABO_3 structures are one of the most important materials because they have high possibility to be used in a wide variety of present day applications. They can be used as dielectric resonators and filters to store and transfer microwave communication signals and can be also used in wireless communication [1,2]. These applications require materials with the following properties :

-High quality (Q) factor (low loss).

-Stable and near zero temperature coefficient of resonance frequency.

- High dielectric permittivity (ϵ_r).

Few materials have all these characteristics. On the one hand, some materials have high dielectric permittivity but they do not have high quality. Ceramics with formula $Ba(B'_{1/3}B''_{2/3})O_3$ are suitable candidates for dielectric resonators at microwave frequencies (5 - 40 GHz) because they have dielectric constants of 20 - 40 and very low dielectric loss. The second condition depends on changing environmental temperatures. The resonance frequency must not change if the environmental temperature changes. The temperature coefficient of the resonance frequency, called τ_r should be reproducible and equal to 0 ± 1 ppm/K . Since the wavelength is inversely proportional to the square root of the dielectric constant, the third requirement reduces the size of the resonator [3,4].

Previous research has been done to study the dielectric properties of $Ba_3Y_{1+x}Nb_2O_9$

where $x = 0, 0.3, -0.07$ and Y= Co, Mg , Zn, Ni. These investigation showed that this material satisfies almost all requirements [5,6,7].

The goal of this thesis is to investigate the effect of the density, chemical composition and the ordering of B-site cations on the dielectric properties of $Ba_{3+y}Co_{1+x}Nb_2O_9$ where $x = 0, 0.3, -0.07$ and y = 0, -0.03. X-ray diffraction and infrared reflectance spectroscopy were the main techniques used.

This thesis is organized as follows : Chapter 2 contains a review of materials used in microwave applications so far and factors influencing their characteristics. Chapter 3 contains a theoretical review of the models which are used to analyze reflectance data. Chapter 4 gives details on the sample preparation as well as density, x-ray diffraction and reflectance measurements. Chapter 5 concentrates on the analysis of the data. Chapter 6 provides conclusions and suggestions for future work.

Chapter 2

Microwave Ceramics

2.1 Perovskite Structure (ABO_3)

The perovskite structure class is one of the most important materials in science. Perovskites are ceramics and comprise the most abundant mineral group in the earth. Perovskite material has the general stoichiometry ABO_3 and consists of a cubic cell with a small ion B at the center with larger A ions situated at the corners, and oxygen ions on the faces as shown in Figure 2.1 [8]. The size of the unit cell distortion depends on the relative values of the ionic radii of A and B ions. The ratio between the size of $R_{(A-O)}$ and size of $R_{(B-O)}$ distance is very important to determine the properties of the materials and is given the name of tolerance factor (t):

$$t = \frac{R_{(A-O)}}{R_{(B-O)}\sqrt{2}} \tag{2.1}$$

where R_{A-O} is the sum of A and O ionic radii and R_{B-O} is the sum of B and O ionic radii. If t is not ≈ 1, structural distortions result and the material is not cubic [8, 9].

In the 1960s Galasso showed that the size and charge of the B ion affects the ordering. If B position is occupied by more than one type of ion, the possibility of ordering of these ions exists along (111) crystallographic planes[10]. The ordered cubic structure has hexagonal symmetry where the hexagonal and cubic lattice parameters are related by $a_h = \sqrt{2}a_c$ and $c_h = \sqrt{3}a_c$ (a_c is cubic lattice.

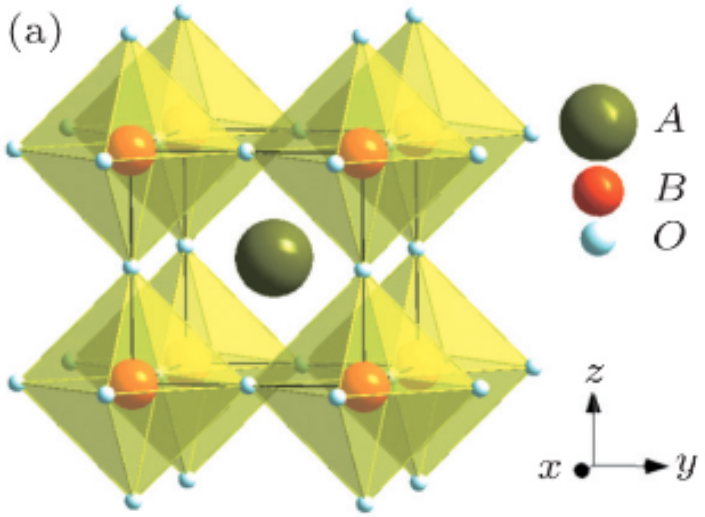

Figure 2.1: perovskite structure[9]

There is long-range ordering with displacement of oxygen ions and repeating sequence $(..., B', B'', B'', B', ...)$ along $< 111 >$ direction of the cubic cell [11]. The long-range cation ordering is facilitated by annealing at higher temperatures for longer durations. Investigations of the structures and electronic properties of the tantalum based system show that at microwave frequency the degree of ordering of B-site cations has an effect on the dielectric loss and increases the Q value from 500 to 35,000 at 10GHz. Figure 2.2 shows the long range B-site cation ordering [12,13].

A number of techniques can demonstrate B-site cation ordering in perovskite materials including far-infrared spectroscopy[15], Raman spectroscopy[16], electron diffraction[17], and X-ray or neutron diffraction [18].

For example the X-ray diffraction pattern reveals the degree of ordering in the intensities of superlattice peaks. The degree of 1:2 ordering can be evaluated by:

$$S = \sqrt{\frac{(I_{100}/I_{110,012,102})_{obs}}{(I_{100}I_{110,012,102})_{cals}}} \tag{2.2}$$

where I_{100} is an integrated intensity of the 100 superlattice reflection and $I_{110,012,102}$ is the integrated intensity of the main 110, 012 and 102 reflections. Note that these peaks are indexed on the hexagonal lattice. If B′ and B" ions

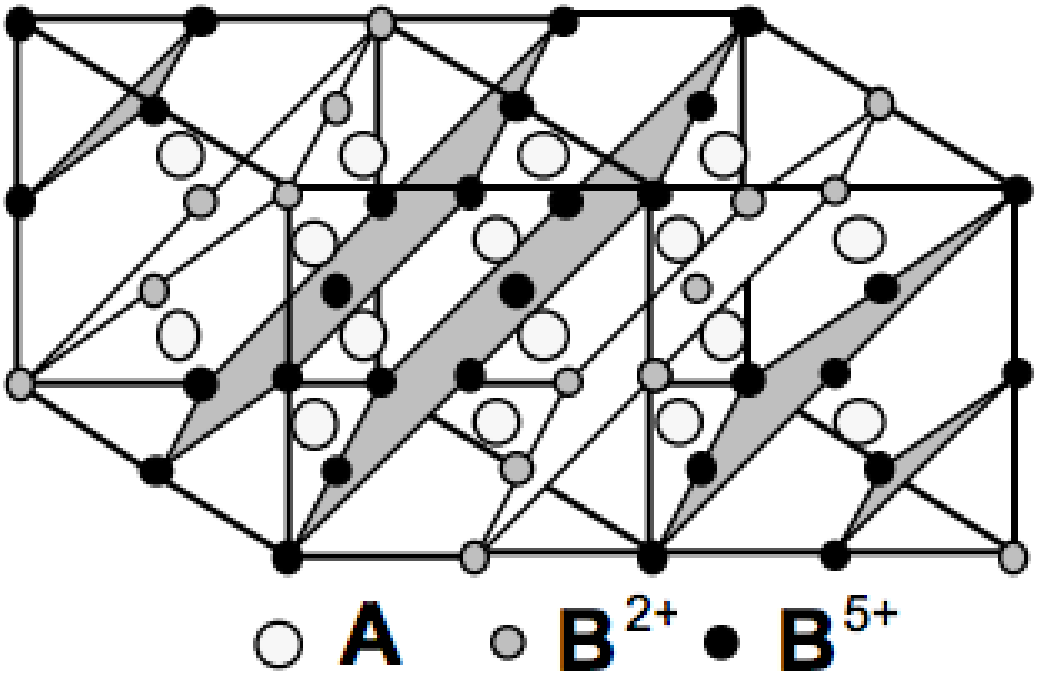

Figure 2.2: 1:2 ordering of perovskite structure[14]

are completely disordered then I_{100}= 0 and the XRD pattern can be indexed using a simple cubic lattice[19].

Fig 2.3 shows an example for 1:2 ordering of $BaMg_{1/3}Nb_{2/3}O_3$ [BMN] ceramic samples. 1:2 Ordering appears as two superlattice peaks, one around 12 degrees (001) and another one around 17 degrees (100). Note that in BMN, the degree of ordering increases with sintering temperature.

2.2 Dielectrics for microwave applications

2.2.1 Dielectric resonator

The principle of operation of the dielectric resonator (DR) is based on Maxwell's theory of electromagnetism [21] When the electromagnetic waves propagate in a medium with relative dielectric permittivity (ϵ) and relative magnetic

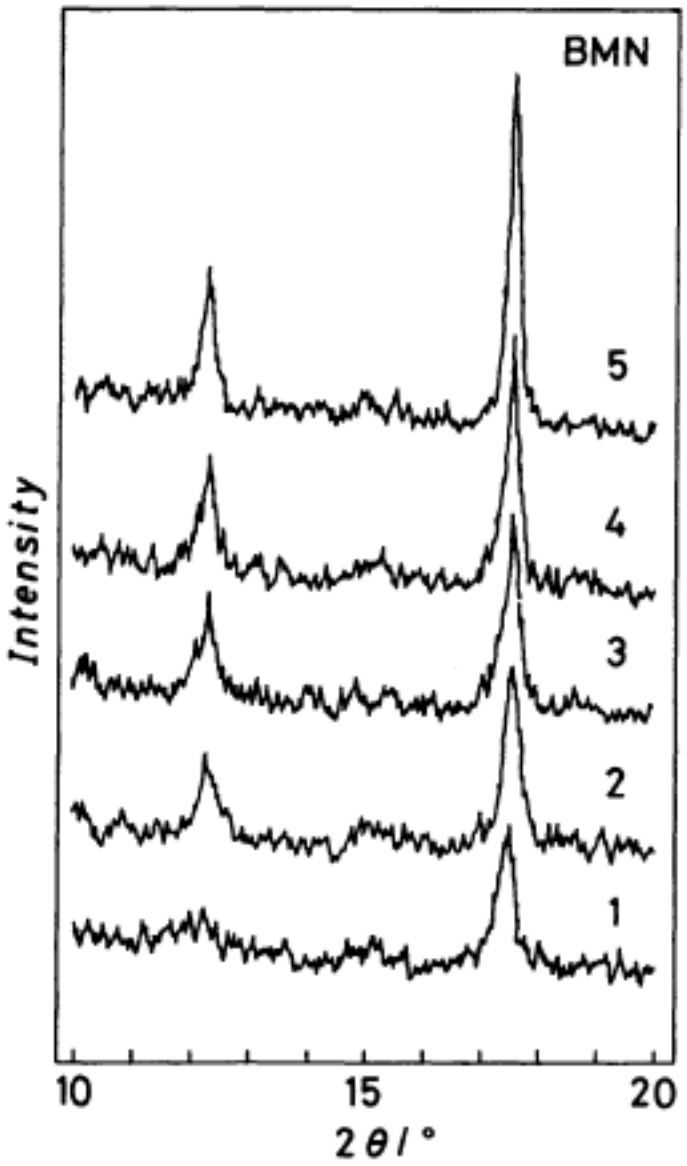

Figure 2.3: X-Ray diffraction patterns of superlattice reflections for Ba ($Mg_{1/3}$ $Nb_{2/3}$) O_3(BMN) samples sintered at temperatures 1. 1473 K , 2. 1573 K , 3. 1673 K, 4. 1773 K and 5. 1833 K [20].

permeability (μ), the wavelength decreases as

$$\lambda = \frac{\lambda_0}{\sqrt{\epsilon\mu}} \tag{2.3}$$

λ_0 is the wavelength in vacuum. Equation 2.3 shows that it is possible to reduce the size of dielectric by factor $\sqrt{\epsilon}$. In 1939, Richtmyer showed that dielectric objects of the appropriate form could function as resonators. Depending on the shape, different resonance modes result [22]. Fig 2.4 shows the distribution of electric and magnetic fields in a cylindrical resonator.

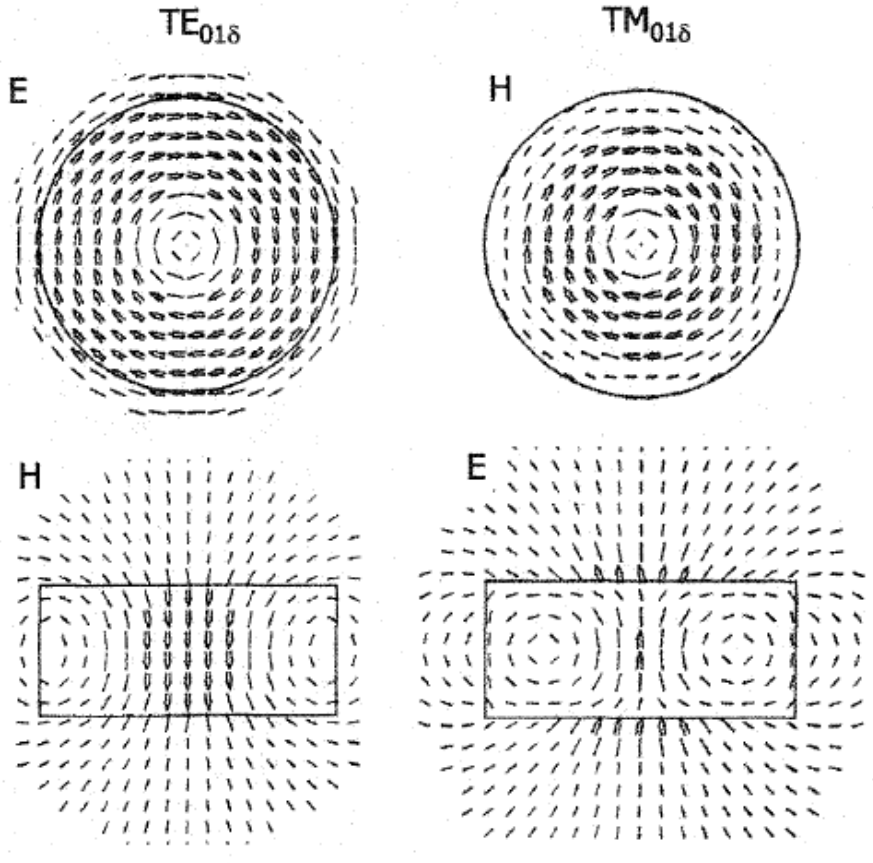

Figure 2.4: The field distribution of electric and magnetic in $TE_{01\delta}$ and $TM_{01\delta}$ mode of cylindrical DR [23]

In the $TE_{01\delta}$ mode inside the cylinder shown in Fig 2.4 the electric field forms simple circles concentric with the axis of the cylinder while the magnetic field looks like a dipole. For high relative dielectric constant the typical dielectric resonator stores more than 60 percent of its magnetic energy and more than 95 percent of its electric energy inside the cylinder[23].

2.2.2 The requirements of the dielectric resonator

The three main requirements for materials utilized as dielectric resonators are:

1. High dielectric constant ϵ ($30 < \epsilon < 100$) to minimize the size of the resonator.

2. High quality factor Q $\approx \frac{\epsilon_2}{\epsilon_1}$($Q > 100$), to optimize frequency selectivity.

3. Small and tunable temperature coefficient of resonance frequency to ensure stability against environmental temperature change. $\tau = -(\frac{1}{2}\tau_e + \alpha_L)$ where $\tau_e = \frac{\partial \epsilon}{\partial T}$ and α_L is the linear expansion coefficient [4].

Dielectric Function

The dielectric permittivity is one of the parameters that impact the reflection of electromagnetic waves at interfaces and the attenuation of wave energy within materials. The complex relative permittivity ϵ can be written as :

$$\tilde{\epsilon} = \epsilon_1 + i\epsilon_2 \tag{2.4}$$

where ϵ_1 is the real part which characterizes the stored energy when the material is exposed to an electric field and ϵ_2 is the imaginary part which characterizes energy absorption and attenuation. The dielectric function of a material is related to the electronic, ionic, and dipolar polarizabilities.

In addition the relative permittivity can be influenced by changing the porosity of the specimens [24].

Q-factor

The quality factor, Q_d, of a dielectric material is define as the inverse of dielectric loss $\tan\delta$:

$$Q_d = \frac{1}{\tan\delta} \approx \frac{\epsilon_1}{\epsilon_2} \tag{2.5}$$

Dielectric losses ($\tan\delta$) depend on disordering or ordering of B site cations, impurities and instability of crystal structure. The total quality factor includes the losses in the waveguide or the resonance cavity Q_w as well as the dielectric loss Q_d[25,26].

$$\frac{1}{Q} = \frac{1}{Q_d} + \frac{1}{Q_w} \tag{2.6}$$

For a resonating system the quality factor is defined as :

$$Q = 2\pi \times \frac{Energy\ stored\ in\ the\ resonance}{Energy\ lost\ per\ cycle} = \frac{\omega_0 W_0}{P} \tag{2.7}$$

where W_0 is the energy stored which is defined as the EM energy stored in the field in the resonator, P is the power dissipation, ω_0 is the resonant frequency [16][17].

Temperature coefficient of resonant frequency

The temperature coefficient of the resonance frequency τ_f is determined by two factors , namely the thermal expansion of material and the temperature coefficient of the dielectric constant τ_ϵ:

$$\tau_f = -\alpha_L - \frac{1}{2}\tau_\epsilon \tag{2.8}$$

The linear thermal expansion α_L is a result of the anharmonicity of the lattice vibrations and ranges between $8 - 15 ppm/K$ for ionic solids. It can be used to offset negative values of τ_ϵ ($-15 ppm/K < \tau_\epsilon < -5 ppm/K$) to solve any changes in the linear size of media [27,28].

The temperature coefficient of the dielectric constant is dependent on the tolerance factor as shown in Fig 2.5 which gives examples for different barium and strontium based compositions where Fig 2.6 lists the acronyms used in the figure.

2.3 Origin of the dielectric loss

The dielectric loss is described by the imaginary component of the permittivity or by tan $\delta = (\frac{\epsilon_2}{\epsilon_1})$. The ratio of the imaginary to the real part of the permittivity depends on the losses in the dielectric medium itself for the microwave resonators[30]. The dielectric loss can be classified into two categories; intrinsic and extrinsic. Intrinsic losses are dependent on the crystal structure and ex-

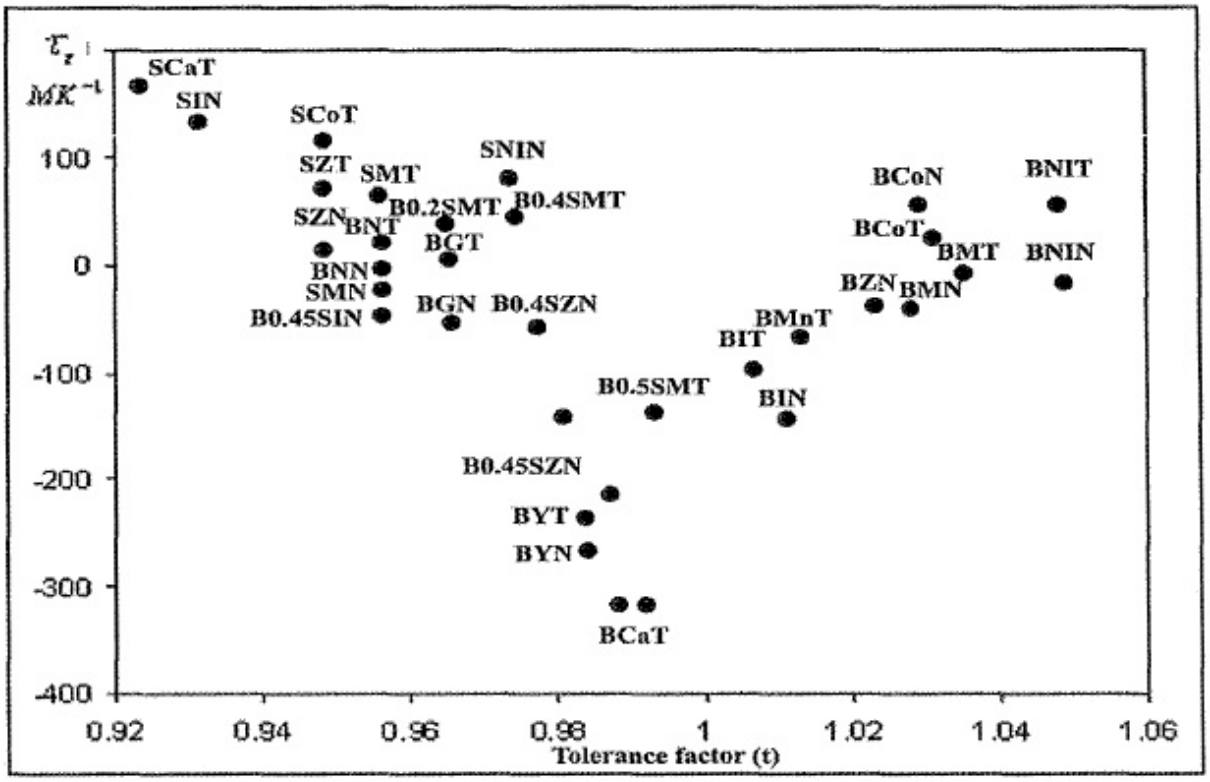

Figure 2.5: The temperature dependence of ϵ, $\tau_\epsilon = \frac{d\epsilon}{dT}$ of some Ba and Sr-based perovskites as a function of the tolerance factor [29]

Abbreviation	Formula	Abbreviation	Formula
B_XSZN	$Ba_XSr_{1-X}(Zn_{1/3}Nb_{2/3})O_3$	$SNiT$	$Sr(Ni_{1/3}Ta_{2/3})O_3$
B_XSMT	$Ba_XSr_{1-X}(Mg_{1/3}Ta_{2/3})O_3$	$BNiT$	$Ba(Ni_{1/3}Ta_{2/3})O_3$
B_XSIN	$Ba_XSr_{1-X}(In_{1/3}Nb_{2/3})O_3$	$BMnT$	$Ba(Mn_{1/3}Ta_{2/3})O_3$
BNT	$Ba\ (Nd_{1/2}Ta_{1/2})O_3$	$BMnN$	$Ba(Mn_{1/3}Nb_{2/3})O_3$
BGT	$Ba(Gd_{1/2}Ta_{1/2})O_3$	$BMgN$	$Ba(Mg_{1/3}Nb_{2/3})O_3$
BYT	$Ba(Y_{1/2}Ta_{1/2})O_3$	$SMgN$	$Sr(Mg_{1/3}Nb_{2/3})O_3$
$BCaT$	$Ba(Ca_{1/3}Ta_{2/3})O_3$	BZT	$Ba(Zn_{1/3}Ta_{2/3})O_3$
$SCaT$	$Sr(Ca_{1/3}Ta_{2/3})O_3$	$BNiN$	$Ba(Ni_{1/3}Nb_{2/3})O_3$
$BCoT$	$Ba(Co_{1/3}Ta_{2/3})O_3$	$SNiN$	$Sr(Ni_{1/3}Nb_{2/3})O_3$
$SCoT$	$Sr(Co_{1/3}Ta_{2/3})O_3$	$BCoN$	$Ba(Co_{1/3}Nb_{2/3})O_3$
SZT	$Sr(Zn_{1/3}Ta_{2/3})O_3$		

Figure 2.6: List of acronyms used in Fig 2.5

ist even in perfect single crystals due to the anharmonic lattice forces and the interaction between the phonons in the crystal [31].

Extrinsic losses are due to single atom defects (many kinds: substitional , vacancies or interstitials) phase impurities, microstructure defects, grain boundaries, porosity, microcracks, random crystallite orientation[32].

Some studies suggest a relation between the grain size and the dielectric losses (for example in alumina where $\tan\delta$ increases with increasing grain size), but they were not systematically coupled in $Ba(Mg_{1/3}Ta_{2/3})O_3$ electroceramics [33].

2.4 Dielectric properties of Ba ($B'_{1/3}B''_{2/3}O_3$) perovskites

The dielectric properties of Ba ($B'_{l/3}B''_{2/3}O_3$) compounds are related to their crystal structure, tolerance factor and the type of order on the B site as well as the A site cation radius. The latter effect can be seen for example when comparing the radii of Ba ($B'_{1/3}B''_{2/3}O_3$and Pb ($B'_{1/3}B''_{2/3}O_3$. The radius of Ba^{2+} is 0.161 nm while for Pb^{2+} it is 0.149 nm while the Q value is 24 and 6500 for for $Pb(Mg_{1/3}Ta_{2/3})O_3$ and $Ba(Mg_{1/3}Ta_{2/3})O_3$ respectively[34].

Different opinions exist concerning the impact of cation ordering on the quality factor [25]. Some research shows that Q does not improve with ordering in $(1-x)Ba(Mg_{1/3}Ta_{2/3})O_3$-$xBaSnO_3$. On the other hand, other investigations showed that there is a relation between the ordering and Q factor. Kawashima reported that Q factor increases with increased ordering structures in ceramics such as $Ba(Zn_{1/3}Ta_{2/3})O_3$[35,36]. Increasing the sintering temperature increases the ordering of the B cations for $Ba(X_{1/3}Ta_{2/3})O_3$[37] .

Chapter 3

Optical properties of solids

Optical methods are very important for the quantitative determination of the energy band structure, impurity levels and localized defects, lattice vibrations and certain magnetic excitations of the material. The dielectric response function of the solid is related to the different types of dipoles, for example permanent molecular dipoles, ionic dipoles that can be excited with infrared radiation or electronic dipoles (inter band transition that can be excited by visible or ultraviolet). This function is significantly modified by changes in temperature or chemical composition. Therefore studying the optical properties is very useful to gain more information about the solid [38, 39]. This chapter discusses one way to measure the optical properties and the models which are used to analyze the data.

3.1 Reflectance

Measuring reflectance is one of the most important methods to measure the dielectric function of a solid. Reflectance (R) is defined as the ratio between the reflected intensity to the incident intensity on the surface and denoted by the symbol R [40].

The interaction between electromagnetic waves and the material can induce transitions between electronic states within the conduction band, between vibrational states or between electronic states in different bands. For non magnetic materials where $\epsilon = \epsilon_o \epsilon_r$ and $\mu = \mu_o$ Maxwell's equations are:

$$\vec{\nabla} \cdot \vec{E} = \frac{\rho_{total}}{\epsilon} \tag{3.1}$$

$$\vec{\nabla} \times \vec{E} = \frac{\partial \vec{B}}{\partial t} \tag{3.2}$$

$$\vec{\nabla} \cdot \vec{B} = 0 \tag{3.3}$$

$$\vec{\nabla} \times \vec{B} = \mu\epsilon \frac{\partial \vec{E}}{\partial t} + \mu \vec{J}_{total} \tag{3.4}$$

where $\vec{E}$ and $\vec{B}$ are the electric and magnetic fields, respectively, ρ_{total} is volume charge density, $\vec{J}_{total}$ is current density, ϵ is permittivity and μ is permeability.

In free space where $\rho_{total} = 0$, $\vec{J}_{total} = 0$, $\epsilon = \epsilon_0$ and $\mu = \mu_0$ the plane wave solution can be written as :

$$\vec{E} = E_0 e^{i(\vec{k}\cdot\vec{r} - \omega t)} \tag{3.5}$$

$$\vec{B} = B_0 e^{i(\vec{k}\cdot\vec{r} - \omega t)} \tag{3.6}$$

where $\vec{k}$ is the wave vector, $\vec{r}$ is the spatial vector ω is the angular frequency and t is time. By substituting this solution in equation 3.2 one obtains :

$$|\vec{B}| = \frac{1}{c}|\vec{E}| \tag{3.7}$$

where c is speed of light which is equal to $\frac{1}{\sqrt{\epsilon_o \mu_o}} = 3 \times 10^8 m/s$.

Consider the electromagnetic wave incident in a medium of permittivity $\epsilon = \epsilon_r \epsilon_0$ and permeability μ_o, the equation 3.7 becomes :

$$|\vec{B}| = \frac{n}{c}|\vec{E}| \tag{3.8}$$

where n is the index of refraction and $n = \sqrt{\epsilon_r}$.

Figure 3.1 shows light incident on an interface between two materials. By applying the boundary conditions at the interface between vacuum or air where $n \approx 1$ and a medium with index of refraction n one finds:

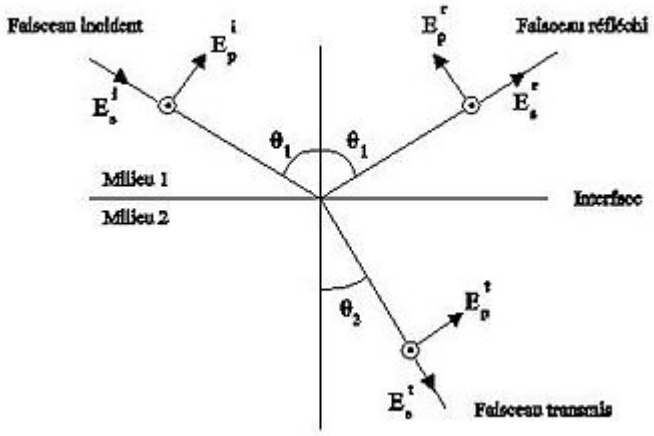

Figure 3.1: The reflection of an electromagnetic wave at the interface between two different media [41]

$$E_i + E_r = E_t \tag{3.9}$$

$$\frac{B_i}{\mu_0} - \frac{B_r}{\mu_0} = \frac{B_t}{\mu_1} \tag{3.10}$$

μ_0 and $\mu_1 \approx \mu_o$ are the magnetic permeability in vacuum and medium, respectively.

Substituting $B_i = \frac{E_i}{c}$, $B_r = \frac{E_r}{c}$ and $B_t = n\frac{E_t}{c}$ in equation 3.10 and and solving the two equations yields:

$$\frac{E_r}{E_i} = \frac{1 - \sqrt{\tilde{\epsilon}}}{1 + \sqrt{\tilde{\epsilon}}} \tag{3.11}$$

The reflectance can be written as :

$$R = \frac{I_r}{I_i} = |\frac{E_r}{E_i}|^2 = |\frac{1 - \sqrt{\tilde{\epsilon}}}{1 + \sqrt{\tilde{\epsilon}}}|^2 \tag{3.12}$$

I_i is the incident light intensity and I_r is reflected light intensity.

The relation between the complex index of refraction $\tilde{n}$ and the complex dielectric function $\tilde{\epsilon_r}$ can be written as :

$$\tilde{n} = \sqrt{\tilde{\epsilon_r}} \tag{3.13}$$

3.1.1 Optical response functions

The propagation of light in the material can be described by the complex dielectric function $\tilde{\epsilon}$ or the complex index of refraction $\tilde{n}$,which are given by :

$$\tilde{\epsilon} = \epsilon_1 + i\epsilon_2 \tag{3.14}$$

$$\tilde{n} = n + ik \tag{3.15}$$

k is the imaginary part of the complex index of refraction which is called the extinction coefficient, related to the amount of absorption loss inside the medium. n is the real part which is also called the refractive index and which is related to the speed of light and the phase velocity $n = \frac{c}{v}$[42]. From equations 3.13, one can derive important relations :

$$\epsilon_1 = n^2 - k^2 \tag{3.16}$$

$$\epsilon_2 = 2nk \tag{3.17}$$

The reflectivity can be written as:

$$R = \left|\frac{1-\tilde{n}}{1+\tilde{n}}\right|^2 = \frac{(n-1)^2 + k^2}{(n+1)^2 + k^2} \tag{3.18}$$

3.1.2 Lorentz model

The Lorentz model for the interaction of the electromagnetic field and a dipole is based on the prototype of the interaction between the electromagnetic wave and a mass-spring system which for example could be the induced dipole on an atom. The electric field will be acting on the electrons by force $(-eE)$ where e is electron charge $(1.6 \times 10^{-19}C)$ and $E = E_0 e^{-i\omega t}$ is the local electric field [43,44].

Electrons react to an electromagnetic field as a damped harmonic oscillator with Hooke's restoring force $-kr$ where k is spring constant and the viscous force $\mathrm{m}\gamma\frac{dr}{dt}$ which depends on the velocity of the electrons.

The equation of motion is given by:

$$m\frac{d^2r}{d^2t} + m\gamma\frac{dr}{dt} + m{\omega_0}^2 r = -eE \tag{3.19}$$

The displacement of the oscillator from equilibrium position $r = r_o e^{-i\omega t}$can be written as :

$$r_o = \frac{1}{m} \cdot \frac{-eE}{{\omega_0}^2 - \omega^2 - i\gamma\omega} \tag{3.20}$$

The dipole moment per unit volume (the polarization P) p is related to r_o and the number of dipole per unit volume(N):

$$P = eNr_o = \frac{Ne^2}{m}\frac{E}{({\omega_o}^2 - \omega^2) - i\gamma\omega} \tag{3.21}$$

Since $\vec{P} = \epsilon_o\chi\vec{E}$, the susceptibility can be written as :

$$\chi = \frac{Ne^2}{\epsilon_o m} \cdot \frac{1}{({\omega_o}^2 - \omega^2) - i\gamma\omega} \tag{3.22}$$

where N is the density of dipole per unit volume.

The quantity $\frac{Ne^2}{\epsilon_o m}$ is the plasma frequency squared ${\omega_p}^2$. Now we can obtain the dielectric function which given by :

$$\tilde{\epsilon}(\omega) = 1 + \chi(\omega) \tag{3.23}$$

$$\tilde{\epsilon}(\omega) = 1 + \frac{{\omega_p}^2}{({\omega_o}^2 - \omega^2) - i\gamma\omega} \tag{3.24}$$

Multiplication of the numerator and denominator of equation 3.24 by $\omega_o^2 - \omega^2 + i\gamma\omega$ gives:

$$\epsilon_1 = 1 + \frac{{\omega_p}^2({\omega_o}^2 - \omega^2)}{({\omega_o}^2 - \omega^2)^2 + (\gamma\omega)^2} \tag{3.25}$$

$$\epsilon_2 = \frac{{\omega_p}^2\gamma\omega}{({\omega_o}^2 - \omega^2)^2 + (\gamma\omega)^2} \tag{3.26}$$

If there is more than one type of oscillator

$$\tilde{\epsilon} = 1 + \Sigma_i \frac{{\omega_{pi}}^2}{{\omega_{oi}}^2 - \omega^2 - i\gamma_i\omega} \tag{3.27}$$

3.1.3 Kramers - Kronig Relation

The Kramers - Kronig relation associates the real and imaginary part of a causal linear response function. In general when a stimulus acts at time t, the linear response is given by [45, 46]:

$$\chi(t) = \int_{-\infty}^{\infty} G(t-t')f(t')dt' \tag{3.28}$$

where $G(t-t')$ is response function and $f(t')$ is the stimulus. $G(t-t')$ is a function of time which describes the response of a system at time t after delta function at time $t = 0$. The definition of the Fourier transform of the response function is:

$$G(t-t') = \frac{1}{2\pi} \int_{-\infty}^{\infty} G(\omega)e^{-i\omega(t-t')}d\omega. \tag{3.29}$$

Applying the Cauchy integral on $G(\omega)$ yields :

$$G(\omega) = \frac{i}{\pi} \int_{-\infty}^{\infty} \frac{G(\omega')}{\omega' - \omega}d\omega' \tag{3.30}$$

where $G(\omega)$ is complex quantity. The real and imaginary parts of this function can be written as :

$$G_1(\omega) = \frac{1}{\pi} P \int_{-\infty}^{\infty} \frac{G_2(\omega')}{\omega' - \omega}d\omega' \tag{3.31}$$

$$G_2(\omega) = \frac{-1}{\pi} P \int_{-\infty}^{\infty} \frac{G_1(\omega')}{\omega' - \omega}d\omega' \tag{3.32}$$

By using the fact that $G_1(\omega)$ is even and $G_2(\omega)$ is odd , applying the integral on only positive ω' and multiplying the integrand of equations 3.31 and 3.32 by $\frac{\omega'+\omega}{\omega'+\omega}$ we get :

$$G_1(\omega) = \frac{2}{\pi} P \int_0^\infty \frac{\omega' G_2(\omega')}{\omega'^2 - \omega^2} d\omega' \tag{3.33}$$

$$G_2(\omega) = \frac{-2\omega}{\pi} P \int_0^\infty \frac{G_1(\omega')}{\omega'^2 - \omega^2} d\omega' \tag{3.34}$$

These equations are called the KK relations where P is the principal value of the integration.

The reflectance in normal incidence can be represented by its phase and amplitude

$$\tilde{r}(\omega) = \frac{E_r}{E_i} = r(\omega) e^{i\theta(\omega)}. \tag{3.35}$$

The reflectance R can be written as :

$$R = |\tilde{r}|^2 = r^2 \tag{3.36}$$

therefore:

$$\ln r(\omega) = \frac{1}{2} \ln R(\omega) + i\theta(\omega) \tag{3.37}$$

by applying K-K relations yields:

$$\theta(\omega) = \frac{\omega}{\pi} P \int_0^\infty \frac{\ln[R(\omega')/R(\omega)]}{\omega^2 - \omega'^2} d\omega' \tag{3.38}$$

By knowing R (the measured spectrum) and θ the real and imaginary parts of the complex index of reflection can be calculated :

$$n = \frac{1 - r^2}{1 + r^2 - 2r cos\theta} \tag{3.39}$$

$$k = \frac{2r sin\theta}{1 + r^2 - 2r cos\theta} \tag{3.40}$$

Eq. 3.38 requires R at all frequency to be known, but the measured range is finite, hence extrapolations are required at both low and high frequency.

3.1.4 Lichtenecker's model

In chapter 5, one will see that the measured reflectance depends on the density of ceramic samples. This is because the sample is an effective medium comprised of air and the sample [47, 48]. The effect has been seen before by Nuzhnyy et al [47]. They prepared samples of $Pb(Mg_{1/3}Nb_{2/3})O_3$ (PMN) of various densities and measured the reflectance as seen in Fig 3.2. Note that the reflectance at $\omega = 300cm^{-1}$ is largest for the highest density. The authors modeled the spectrum using Lichtenecker's model.

In 1926 Lichtenecker suggested the effective medium model:

$$\tilde{\epsilon}_{eff} = (\sum_{i=1}^{N} X_i \tilde{\epsilon_i}^{\alpha})^{\frac{1}{\alpha}} \tag{3.41}$$

where α is constant, X_i is the fraction and $\tilde{\epsilon}_i$ are the relative electrical permittivity of component.

$$\sum_i X_i = 1 \tag{3.42}$$

$$\tilde{\epsilon}^{\alpha}_{eff} = [(1-P)\tilde{\epsilon}^{\alpha}_1 + p\tilde{\epsilon}^{\alpha}_{air}] \tag{3.43}$$

$$\tilde{\epsilon}^{\alpha}_{eff} = [(1-P)\tilde{\epsilon}^{\alpha}_1 + p] \tag{3.44}$$

Note that Fig 3.2 shows the reflectance of PMN can be modeled if $\alpha = 0.2$ letting p change.

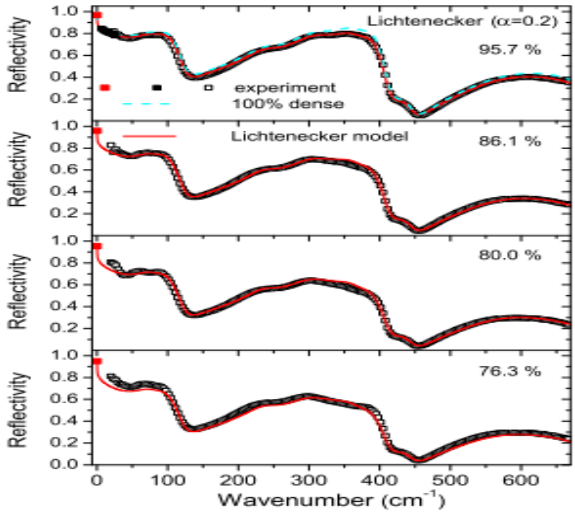

Figure 3.2: Example of fitting using Lichtenecker's model [47]

Chapter 4

Experimental Methods

4.1 Preparing samples for optical measurement

4.1.1 $Ba_3Co_{1+x}Nb_2O_9$ Ceramic preparation

Ten ceramic samples $Ba_3Co_{(1+x)}Nb_2O_9$ [BCN] where $x = -0.07, 0.03$ and 1 were made at McMaster university by PhD student Dmytro Grebennikov as well as one of $Ba_{2.97}CoNb_2O_9$. These samples were made in two steps. During the first step, the corresponding columbites of $Co_{1+x}Nb_2O_6$ were synthesized at calcination temperatures 1150 °C. During the second step, after adding the corresponding amount of $BaCO_3$ the final material was sintered for 8 hours in different temperatures between 1200° C to 1500° C [49].

The chemical reactions of the sample preparation were as follows:

a. Nonstoichiometry on Ba-site

$2Co_3O_4 + 6Nb_2O_5 \longrightarrow 6CoNb_2O_6 + O_2$

b. Nonstoichiometry on Co site

$2(1+x)\ Co_3O_4 + 6Nb_2O_5 \longrightarrow 6Co_{1+x}\ Nb_2\ O_6 + (1+4x)O_2$

An appropriate amount of barium carbonate was added to the columbite samples during the second stage:
a. Nonstoichiometry on Ba site

$$2CoNb_2\ O_6 + 6(1+y)BaCO_3 \longrightarrow 2Ba_{3+3y}\ CoNb_2\ O_9 + 6(1+y)CO_2 + 3yO_2$$

b. Nonstoichiometry on Co site

$$Co_{1+x}Nb_2\ O_6 + 3BaCO_3 \longrightarrow Ba_3\ Co_{1+x}Nb_2\ O_9 + 3CO_2$$

To obtain a highly reflecting surface and good optical measurements, the BCN samples were polished down during three steps. During the first step samples were polished down by a 600 grit size sandpaper using kerosene as lubricant. During the second step, the samples were polished down using 6μm diamond paste and Buehler Metadi lubricant. During the third step these samples were polished down to the smooth final surface that was produced by 1μm diamond paste and again Buehler Metadi lubricant. Between each step the samples were cleaned using ultra sound machine for one hour in acetone, to remove polishing grit.

4.1.2 X-ray Diffraction Basics

Laue's equation

From Fig 4.1 the path difference between the rays [50]:

$$dcos\theta + dcos\theta' = \vec{d} \cdot (\hat{n} - \hat{n}') = m\lambda \tag{4.1}$$

Multiply through by $2\pi/\lambda$:

$$d \cdot (\vec{k} - \vec{k'}) = 2\pi m \tag{4.2}$$

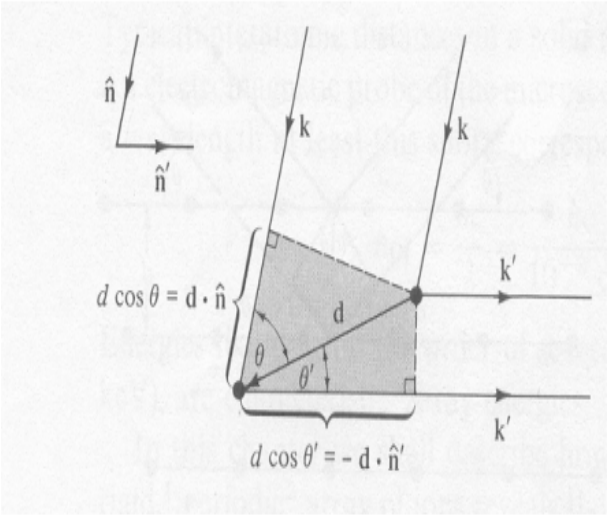

Figure 4.1: X-ray diffraction [50]

for the Bravais lattice of scatterers, where $\vec{d}$ is a direct lattice vector($\vec{d} = \vec{R}$).

$$\vec{R} \cdot (\vec{k} - \vec{k'}) = 2\pi m \tag{4.3}$$

Multiply by i and raise to power of e.

$$e^{i(\vec{k}-\vec{k'})\cdot\vec{R}} = e^{i2\pi m} = 1 \tag{4.4}$$

So, $\vec{k'} - \vec{k} = \vec{G}$ and strong diffraction occurs when the change in wave vector, $\vec{k'} - \vec{k}$, is a vector of the reciprocal lattice. The distance between successive planes is :

$$|\vec{G_0}| = \frac{2\pi}{d} \tag{4.5}$$

G is integral multiple of G_0

$G = nG_0$

therefore

$G = \frac{2n\pi}{d}$

$G = 2ksin\Theta$

Bragg's Law

For elastic scattering $|\vec{k}| = |\vec{k'}|$ [51].

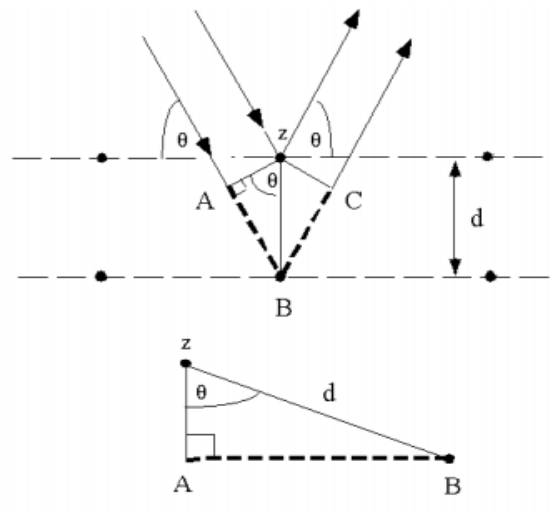

Figure 4.2: Bragg's Law [51]

From Fig 4.2

$$n\lambda = AB + BC = 2AB \tag{4.6}$$

$$sin\theta = \frac{AB}{d} \tag{4.7}$$

$$AB = dsin\theta \tag{4.8}$$

Therefore:

$$n\lambda = 2dsin\theta \tag{4.9}$$

For the disordered cubic structure:

$\frac{1}{d^2} = \frac{h^2+k^2+l^2}{a^2}$

For the ordered hexagonal structure:

$\frac{1}{d^2} = \frac{4}{3}\frac{h^2+hk+k^2}{a^2} + \frac{l^2}{c^2}$

X-Ray measurment

X-ray measurement were done using the Rigaku Smart Lab in the parallel beam optic (PB) mode which is shown in fig 4.3. 1:2 ordering in samples is demonstrated if superlattice peaks appear around 12 and 17 degrees as discussed in section 2.1.

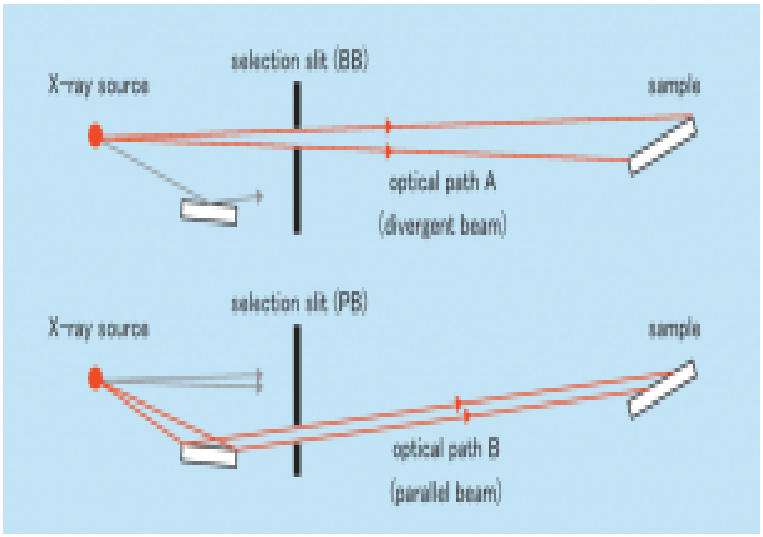

Figure 4.3: Schematic diagram of PB method [52]

4.2 Density measurements

The densities of the sintered samples were measured using two different methods.

Geometric method

The volume was measuring by using a micrometer to measure the thickness and the radius[53]. The value of the volume was calculated according to

$$V = \pi r^2 \times t \tag{4.10}$$

where r is radius and t is the thickness of the sample. The uncertainty can be calculated according to

$$\frac{\Delta\rho}{\rho} = \sqrt{[\frac{\partial\rho}{\partial t}\Delta t]^2 + [\frac{\partial\rho}{\partial r}\Delta r]^2 + [\frac{\partial\rho}{\partial m}\Delta m]^2} \tag{4.11}$$

Archimedes' method

The mass of sample in air = m

The mass of sample in liquid = m′

The displaced mass= m - m′ By knowing density of liquid one can calculate the volume of sample:

First measurement : m

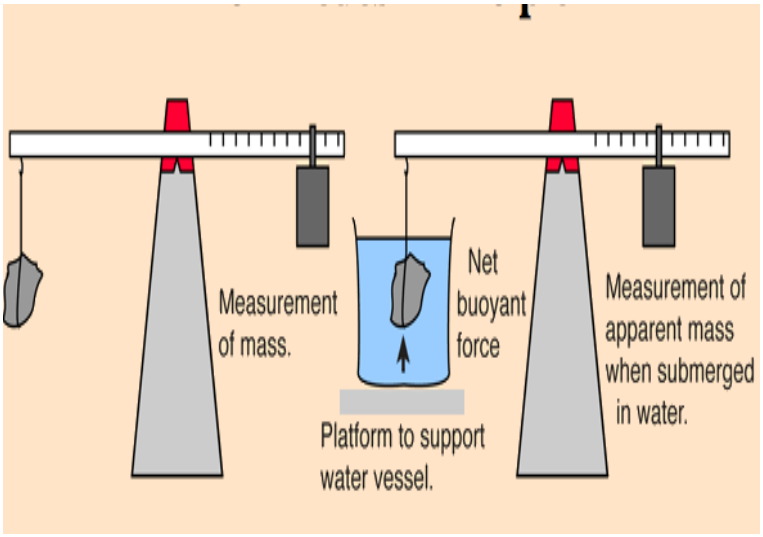

Figure 4.4: Archimedes method diagram [54]

Second measurement: m′ = m-$\rho_L V$

where ρ_L is density of liquid

Therefore V of sample V = $\frac{m-m'}{\rho}$

The density of sample is

$$\rho = \frac{m}{V} = \frac{m}{m-m'}\rho_L \tag{4.12}$$

The uncertainty is the standard deviation of a number of measurements

The liquid used in experiment is Toluene [$C_6H_5CH_3$](density is 0.8669 g/cm^3)[54, 55].

4.3 Reflectance measurement

The Bruker IFS66\V infrared spectrometer is used to measure the infrared (50-5000 cm^{-1}) optical reflectance of the BCN samples.

4.3.1 Interferometer

The Michelson interferometer consists of two basic parts. The first part consists of two mirrors, one is moving and other is fixed while the second part is a beamsplitter. The beamsplitter used depends on the frequency range one wants to measure. OPUS IR software is used to control the interferometer.

OPUS IR controls the velocity of the moving mirror, the number of scans and the resolution. Some calculations can be done such as division or subtracting spectra.

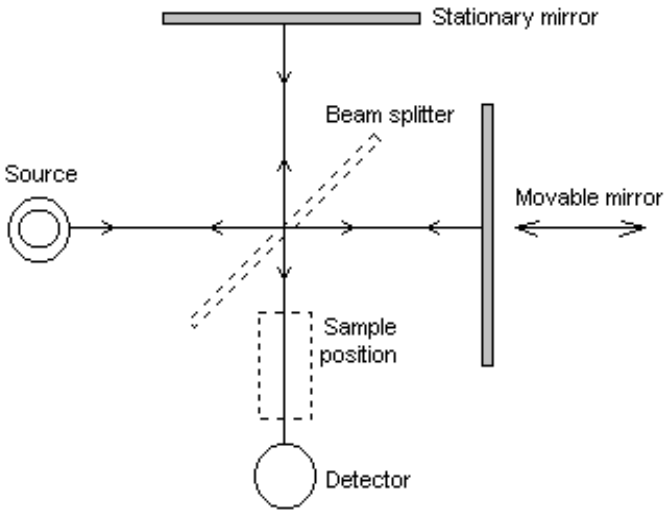

Figure 4.5: Michelson Interferometer [56]

Fig 4.5 shows the diagram of the Michelson interferometer in the Bruker IFS-66V. A broad frequency-band[(50 -cm^{-1} - 5000 cm^{-1} cermet) or (2000 cm^{-1}- 20000 cm^{-1} tungsten halogen)] beam of the light is emitted from the source and strikes the beam splitter where it splits the beam by transmitting half and reflecting the other half. The fixed mirror reflects the reflected beam whereas the transmitted beam strikes the moving mirror. Both beams have approximately the same intensity . The returning beams are added at the beam splitter. The path difference between the two beams depends on the motion of the moving mirror. The total change in path from zero path position where two beams travel equal paths can be written as :

$$\delta = 2d \tag{4.13}$$

where d is the distance the mirror moves. When the path difference is an integer number of the wave lengths constructive interference occurs :

$$\delta = 2d = m\lambda, m = 1, 2, 3, ... \tag{4.14}$$

When the path difference is integral number plus half the wave length is

called destructive interference which can be written as :

$$\delta = 2d = (m + \frac{1}{2})\lambda \tag{4.15}$$

Fig 4.6 shows an example intereferogram. The intereferogram is large when the difference between paths is zero. An example power spectrum is determined by Fourier transformation of the intereferogram is shown Fig 4.7.

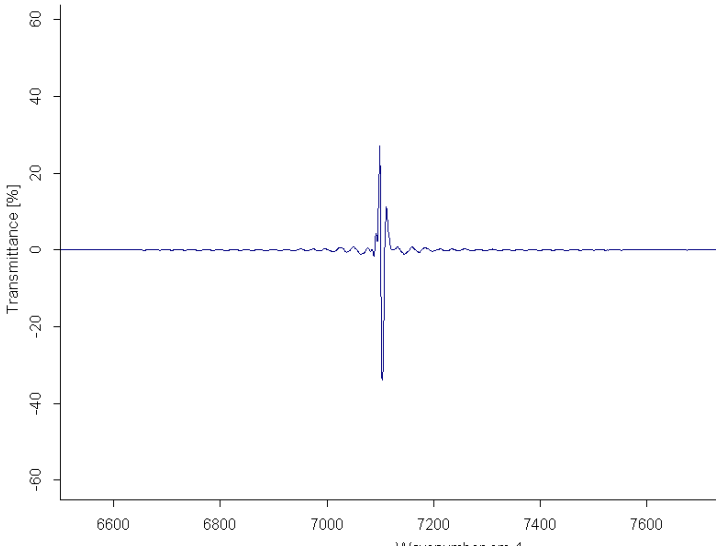

Figure 4.6: Sample intereferogram . Horizontal axis in units: cm^{-1}

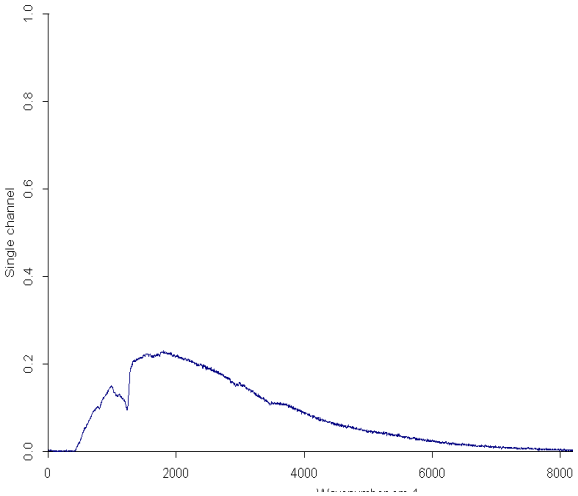

Figure 4.7: Sample spectrum [MCT detector, MIR lamp (cermet) KBr beam splitter, resolution 4 cm^{-1}]. Horizontal axis in units: cm^{-1}

4.3.2 The sample chamber

The sample chamber has three important parts: The sample holder, the gold evaporating coils and the cooling finger of the Janis cryostat. The sample holder is connected to the cooling finger.

Figure 4.8: The sample and reference attached to cold finger

Fig 4.8 shows the design of the head of the sample holder made out of copper. On the right, note the sample and on the left the reference.The Janis cryostat is mounted on a linear translator to move between the sample and reference (mirror). The linear translator is software controlled. For experiments depending on the temperature, liquid helium is made to flow through the Janis cryostat. The thermal grease was used to contact between the sample holder and the cold finger.

A background spectrum was measured with the reference mirror and saved at the beginning of each experiment. A second reference spectrum divided by the background spectrum signal produce the one hundred percent line. The reference and the sample reflectance can be calculated as:

$$r_r = \frac{Reference}{Background} \tag{4.16}$$

$$r_s = \frac{sample}{Background} \tag{4.17}$$

r_r is measured to acouunt for drift in detector sensitivity and or source intensity.

Fig 4.9 shows the reflectance of the sample r_s. Fig 4.10 shows the reflectance of the gold coated sample r'_s defined below.

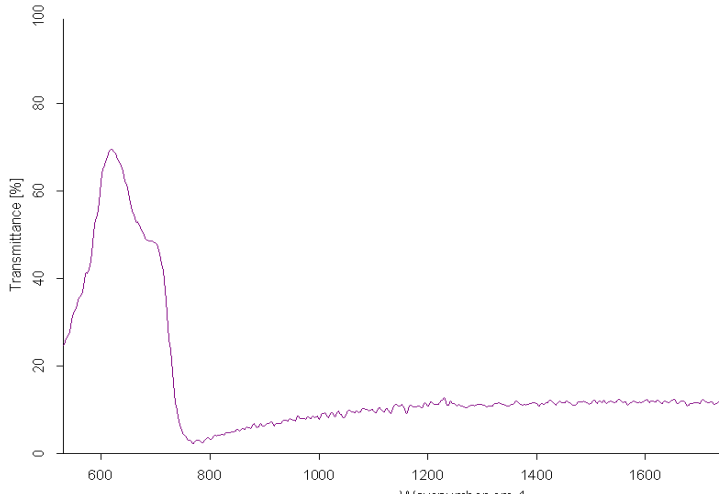

Figure 4.9: The reflectance vs frequency (cm^{-1} [r_s])of the sample in MIR.

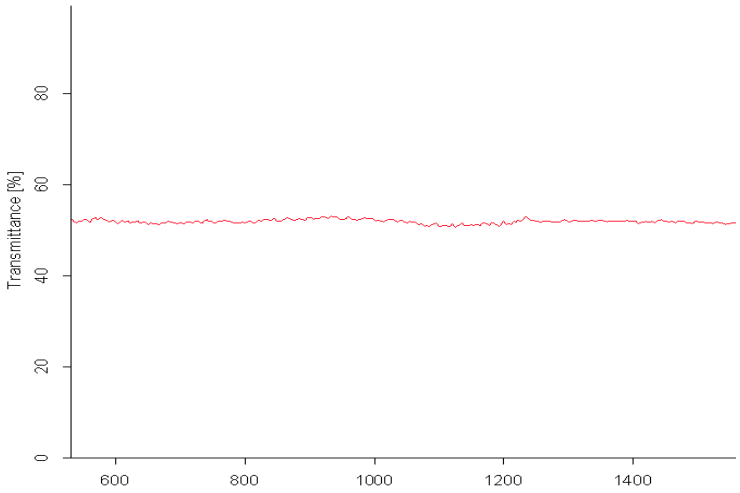

Figure 4.10: The reflectance versus frequency (cm^{-1}) of the sample in MIR gold coated (r'_s). Note that we changed the gain because the signal became too large and detector was saturating after evaporation of gold.

To evaporate the gold, the sample is moved by linear translator to the front of the tungsten coils. Three gold rings made from approximately 4 mm of wire of diameter were hung from the coil. Gold was evaporated onto the sample to account for any impact of the surface roughness of the sample on the optical reflectance. Two steps of power used. In the first, a power of about $25V \times 1Amp$ was applied for two seconds. In the second step a power $25V \times 2Amp$ was applied

Range (cm^{-1})	Beam splitter	Detector	Window	Source
50 - 600	$6\mu m$ Mylar with Ge	Bolometer 4.2 K	Polypropylene	Globar (MIR)
500 - 6000	Ge on KBr	MCT	KBr	Globar (MIR)
1000-12000	Ge on KBr	MCT	KBr	Tungsten (NIR)

Table 4.1: Optical components used in different portions of the spectrum

for 40 seconds. The reflectance of the sample after evaporating the gold was measured:

$$r_s' = \frac{Goldcoatedsample}{Background} \tag{4.18}$$

The absolute reflectance of the sample can be written as :

$$R_{abs} = \frac{r_s}{r_r} \cdot \frac{r_r^{'}}{r_s^{'}} \cdot r_{Au} \tag{4.19}$$

If there were no detector or source intensity drift then $r_r^{'} = r_r$. Also r_{Au} is reflectance of gold (we used $r_{Au} \approx 1$).

4.3.3 Optical components

The spectrometer is designed to attach different components depending on the spectral range. Three different ranges of frequency can be measured. The light source of the far infrared and mid infrared ranges was a globar lamp (cermet) and for near infrared and visible ranges was a tungsten lamp. Table 4.2 shows the combination of windows detectors and beam splitter for each range.

Chapter 5

Results and discussion

5.1 X-Ray

Figure 5.1 shows x- ray diffraction (XRD) pattern for $Ba_3Co_{0.93}Nb_2O_9$ sintered at different temperatures. As shown the samples have weak 1:2 ordering which appears in small peaks at degree 17.6 and 12.5.

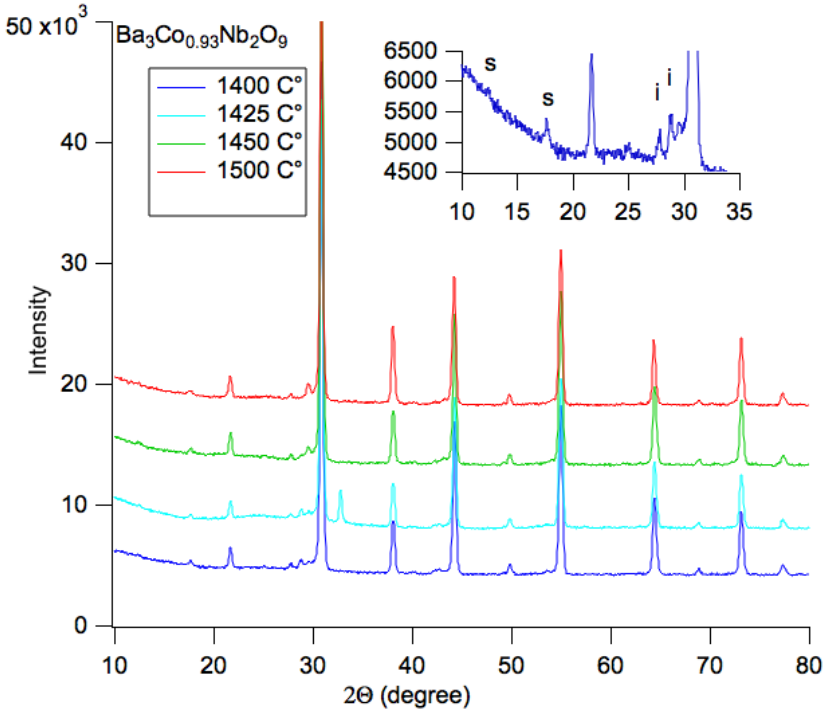

Figure 5.1: X-ray spectrum of $Ba_3Co_{0.93}Nb_2O_9$ samples made in different sintered temperature. Inset: s is super lattice peak and i is an impurities peak

Figure 5.2 shows the XRD pattern for $Ba_3Co_{1.03}Nb_2O_9$ samples sintered at different temperature. All samples have order as shown by the small peak near

17° in Fig 5.1 and 5.2. All samples have impurities which we can noted that by extra peaks around 28°.

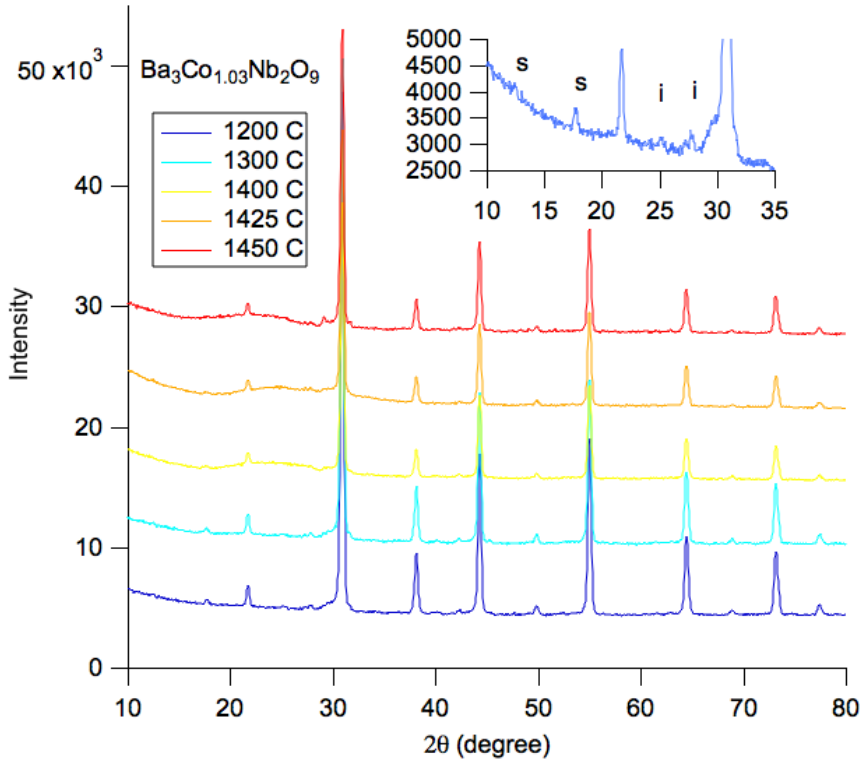

Figure 5.2: X-ray spectrum of $Ba_3Co_{1.03}Nb_2O_9$samples made in different sintered temperature. Inset: s is super lattice peak and i is an impurities peak of $Ba_3Co_{1.03}Nb_2O_9$ sintered at temperature of 1200°C.

5.1.1 Measurement of relative degree of ordering

The degree of ordering can be obtained by using this relation:

$$S = \sqrt{\frac{(I_{100}/I_{110,012,102})_{obs}}{(I_{100}/I_{110,012,102})_{calc}}} \tag{5.1}$$

where$(I_{100}/I_{110,012,102})_{obs}$ is the ratio of the integrated intensity of the (100) superlattice reflection at 17.6 ° to that of (110,012,102) main reflection at 30.2°, and $(I_{100}/I_{110,012,102})_{calc}$ is the calculated value for a completely ordered structure which can be determined by using :

$$I_{hkl} = KM|F_{hkl}|^2 L_P \tag{5.2}$$

where K is a constant, F_{hkl} is the structure factor for the (hkl) reflection, M is the multiplicity factor for (hkl) reflection, and Lp is the Lorentz polarization factor.

Because we donot have the calculated value (the denominator of eq 5.1), S′ the relative degree of ordering was determined:

$$S' = \sqrt{\frac{N_1}{N_2}} \tag{5.3}$$

We calculated (total counts - trapezoid area between the black lines as shown in fig 5.3 for 10 values of different widths.

N_1 between : 17.458-18.024 deg and 16.986→18.496 deg

N_2 between : 30.202-31.665 deg and 29.682→32.137 deg

The values listed in table 5.1 are the mean values and the uncertainty is the standard deviation. Fig 5.3 compare the superlattice peaks for three samples with three different S′ values.

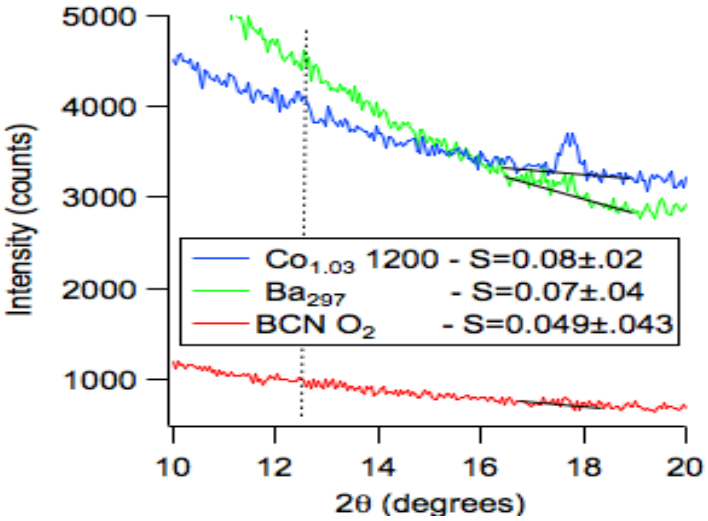

Figure 5.3: Calculating the degree of ordering

A comparison of ordering between samples is shown in table 5.1, $S' = \sqrt{\frac{I_{100}(17.6°)}{I_{110}(30.9°}}$). Note that $Ba_3Co_{1+x}Nb_2O_9$ where x≠0 exhibit larger value than x =0.

Fig 5.1 shows there is no change in structure by change in sintering temperature. The XRD pattern shows the samples have impurities which are indicated by peaks near 25° and 29° in the inset. These peaks are for another material

Sample Name	Sintering temperature (C°	S′(relative degree of ordering)	Geometric method $\rho_g(g/cm^3)$	Archimedes method $\rho_a(g/cm^3)$
$Ba_3Co_{0.93}Nb_2O_9$	1400	0.09± 0.02	Irregular shape	6.04± 0.01
$Ba_3Co_{0.93}Nb_2O_9$	1425	0.09± 0.02	6.03 ± 0.06	6.29 ± 0.01
$Ba_3Co_{0.93}Nb_2O_9$	1450	0.09± 0.02	6.04 ±0.06	6.38± 0.01
$Ba_3Co_{0.93}Nb_2O_9$	1500	0.09± 0.02	6.20 ± 0.02	6.31 ± 0.01
$Ba_3CoNb_2O_9$	1500	0.06± 0.03	Irregular shape	6.08 ± 0.01
$Ba_3Co_{1.03}Nb_2O_9$	1200	0.09± 0.01	5.41 ± 0.02	6.05 ± 0.01
$Ba_3Co_{1.03}Nb_2O_9$	1300	0.09± 0.01	6.00 ± 0.01	6.17± 0.01
$Ba_3Co_{1.03}Nb_2O_9$	1400	0.09± 0.03	6.04 ± 0.02	6.23± 0.01
$Ba_3Co_{1.03}Nb_2O_9$	1425	0.09± 0.03	Irregular shape	6.25 ±0.02
$Ba_3Co_{1.03}Nb_2O_9$	1450	0.07± 0.02	Irregular shape	6.22 ±0.01
$Ba_3CoNb_2O_9$ (O_2)	-	0.049± 0.043	6.32 ± 0.01	6.34 ± 0.02
$Ba_{2.97}CoNb_2O_9$	1445		6.29 ± 0.02	6.34 ± 0.03

Table 5.1: Density and degree of ordering

not for BCN perovskite ceramic. The sample sintered at 1425°C also has an extra peak around 31°.

5.2 Density Data

The density data of the samples are listed in Table 5.1. Note that the density is correlated with sintering temperature and the density measured using Archimedes' method is higher than density measured using the geometric method. This is because the geometric volume includes open pores which are excluded in Archimedes' method. The uncertainty for density data depends on the method used. The uncertainty using the geometric method is a little bit higher than the uncertainty using Archimedes' method. For the geometric method a couple of samples could not be measured because they have irregular shape.

5.3 Reflectance

The reflectance of the BCN(cubic and hexagonal) ceramic samples made with different sintering temperature and different concentration of Cobalt was measured in the spectral range between 50 cm^{-1} to 5000 cm^{-1}. This work studied three important variables that affect the reflectance spectra : density, chemical composition and degree of 1:2 order. Fig 5.4 shows the reflectance of BCN sample in the range of the optical phonons (FIR and MIR ranges). The full spectral range data is shown in figure 5.5. Note that the ceramic sample has a typical insulator reflectance with well defined phonons this range.

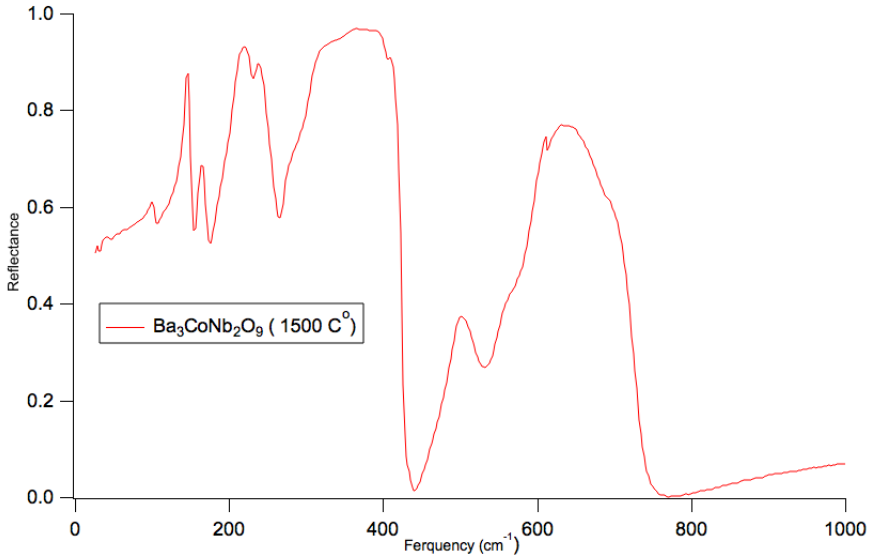

Figure 5.4: The far infrared reflectance of Ba $_3CoNb_2O_9$ sample sintered at a temperature of 1500°C

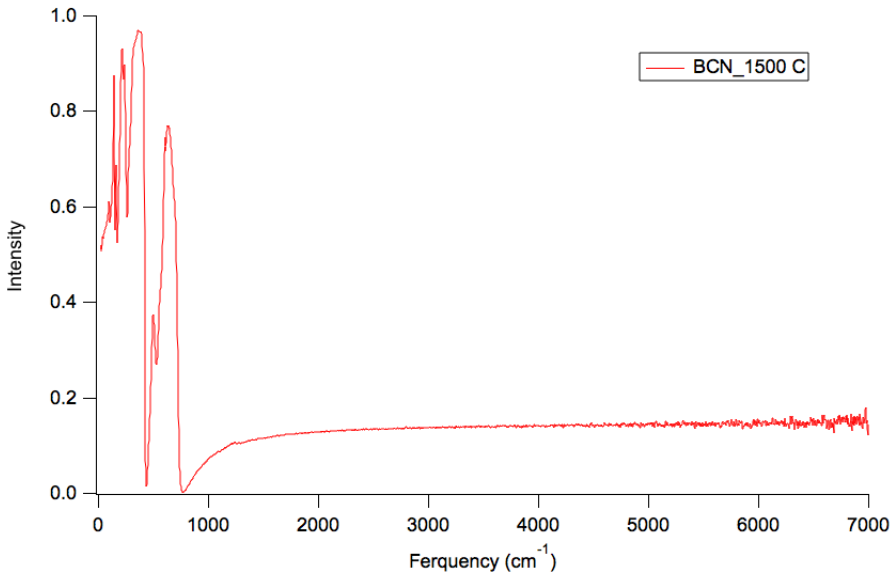

Figure 5.5: The full spectral range of Ba_3 $CoNb_2O_9$ sample sintered at a temperature of 1500°C

5.3.1 Effect of density I

Fig 5.6 shows the reflectance for $Ba_3Co_{0.93}Nb_2O_9$ samples sintered at different temperatures in the FIR part of the spectrum. The sample made at the lowest sintered temperature (which also has the lowest density) has lower reflectance compared with the sample made at the highest sintering temperature (and highest density).

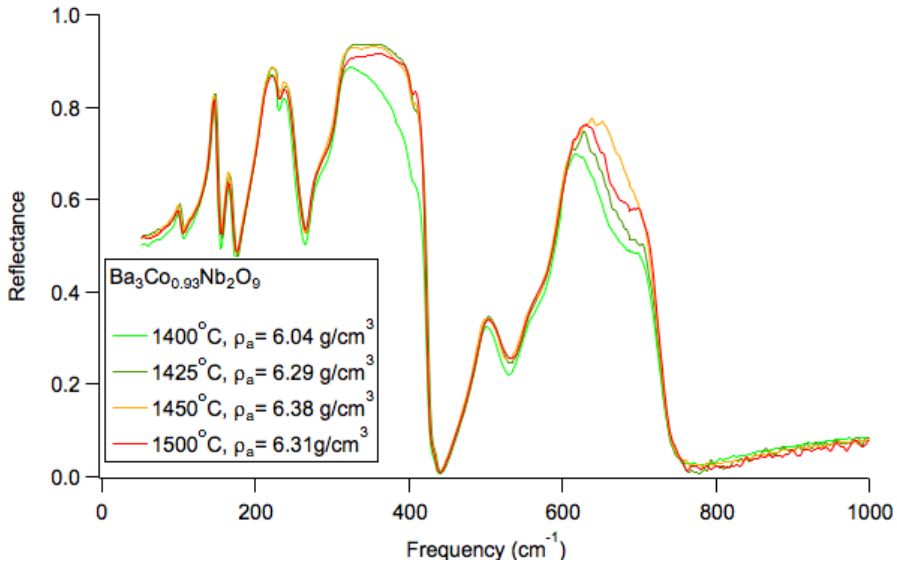

Figure 5.6: Reflectance of $Ba_3Co_{0.93}Nb_2$ O_9 samples sintered at different temperatures. The density in the legend was measured using the Archimedes method

Figure 5.7 shows the reflectance of the samples of $Ba_3Co_{1.03}Nb_2O_9$ sintered at different temperatures. Again note that the sample sintered at the highest temperature has the highest reflectance.

As will be explained in section 5.3.4, the dependance of the reflectance on density can be explained using the Lichtenecker effective medium model.

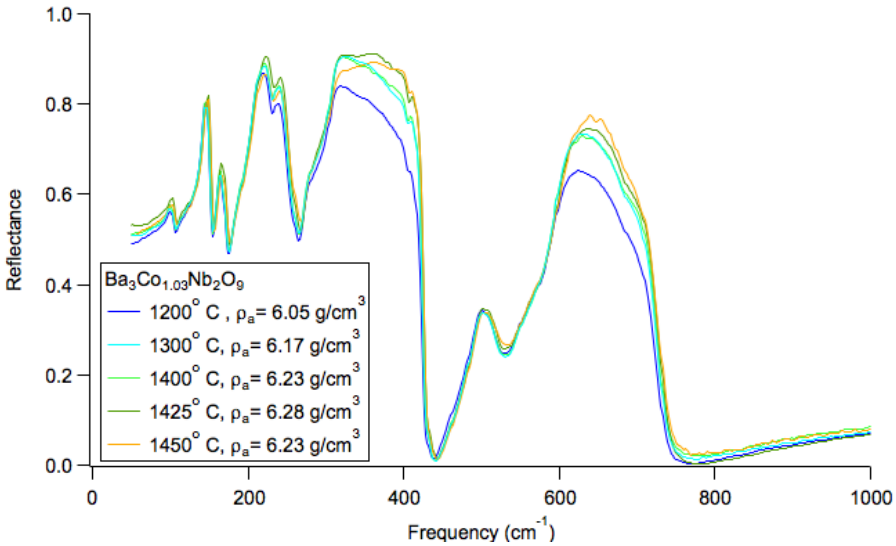

Figure 5.7: Reflectance of $Ba_3Co_{1.03}Nb_2O_9$samples sintered at different temperature. The density in the legend was measured using the Archimedes method

5.3.2 Lorentz oscillator model

Fig 5.8 shows a sample fit of reflectance data for $Ba_3Co_{0.93}Nb_2O_9$ sintered at a temperature of 1450°C of the reflectance data using the Lorentz model (Eq.3.27) with parameters listed in table 5.2. The parameters for the other samples are listed in Appendix A. The high frequency dielectric constant ϵ was between approximately 4.8 to 5.3 for all samples. The dielectric functions determined using the Lorentz model were used to generate low frequency extrapolations for Kramers-Kronig analysis and to estimate ϵ_1 and the loss at microwave frequencies (0.01 cm^{-1}- 0.1 cm^{-1}).

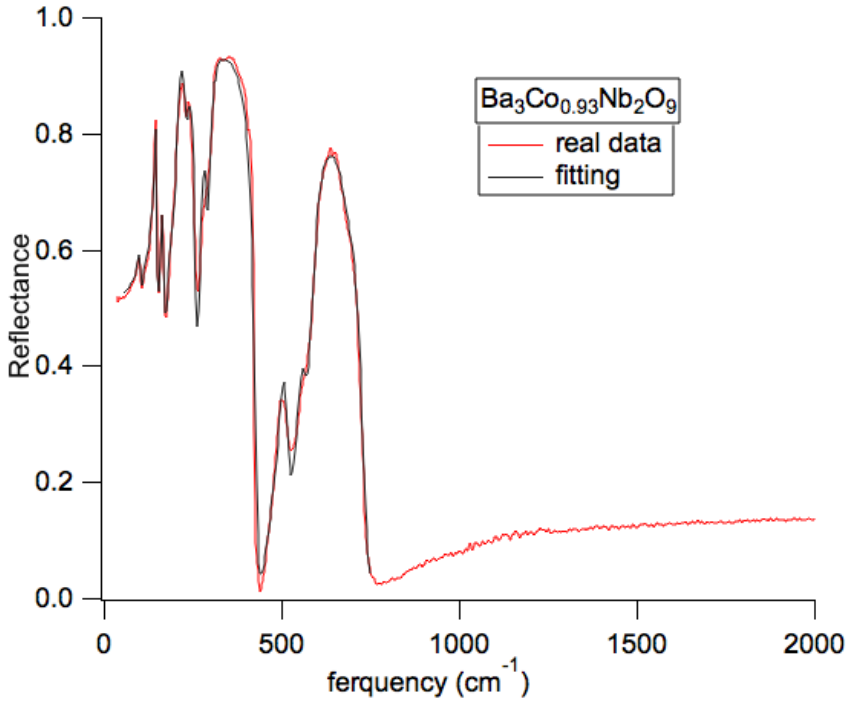

Figure 5.8: Reflectance and fitting of the $Ba_3Co_{0.93}Nb_2O_9$ sample made at a sintering temperature of 1450° C

5.3.3 Kramers -Kronig analysis

Determination of the optical conductivity was done by using Kramers-Kronig (KK) relations. The KK phase integral (eq 3.38) requires data at all frequencies but, the measurements in this work cover a limited range of the spectrum.

For low frequencies (1cm^{-1}- 70 cm^{-1}) we used the extrapolated the Lorentz model of the reflectance. Fig 5.9 shows sample low frequency data as a blue

Oscillator number	ω_0	Γ	ω_P
1	102± 1	86± 4	107 ±30
2	144.7±0.5	4.4± 0.8	356± 10
3	165± 1	10 ± 2	294 ± 20
4	211 ±1	8± 1	753 ± 20
5	235 ± 2	15 ± 4	278 ± 40
6	278 ± 1	16 ± 2	447± 20
7	300± 1	14± 2	411± 20
8	-	-	-
9	503 ± 1	25 ± 3	333 ± 10
10	557± 1	27 ± 5	349± 30
11	591 ± 1	30 ± 2	552 ± 20
12	686 ± 7	40 ± 20	54 ± 20

Table 5.2: The Lorentz model parameters for $Ba_3Co_{0.93}Nb_2O_9$ sintered at temperature 1450° C

line.

Between 7000 cm^{-1} and 120000 cm^{-1} two possible model reflectances were used. One expects the reflectance to have several peaks due to inter band transitions in this frequency range. We choose to study two different models to estimate the uncertainty in K-K ϵ_1 and σ_1. Model I [Fig 5.10] had one strong Lorentz oscillator. Model II [Fig 5.11] had two Lorentz oscillators. The model parameters were chosen so that the reflectance matched with the measured data near 7000 cm^{-1} and also the X-Ray reflectivity as shown in figures 5.10 and 5.11. The x-ray reflectivity shown in Fig 5.12 was generated using the method discussed by D. B. Tanner[57].

5.3.4 Effect of density II

Fig 5.13 shows how the effect of the density can be explained using Lichtenecker model. For the Lichtenecker model, the $\tilde{\epsilon}$ parameters of the highest density sample were used. If alpha and the porosity (p) were free parameters for the fit between 50 and 1500 cm^{-1}, it is found α =0.20+/-0.04 and p=0.075+/-.004. This is about the porosity found from the Archimedes density. If you fix p=0.17 (the geometrical density) you get about the same goodness of fit, but a different α value. That shows p and α are not independent parameters. In Fig 5.13,

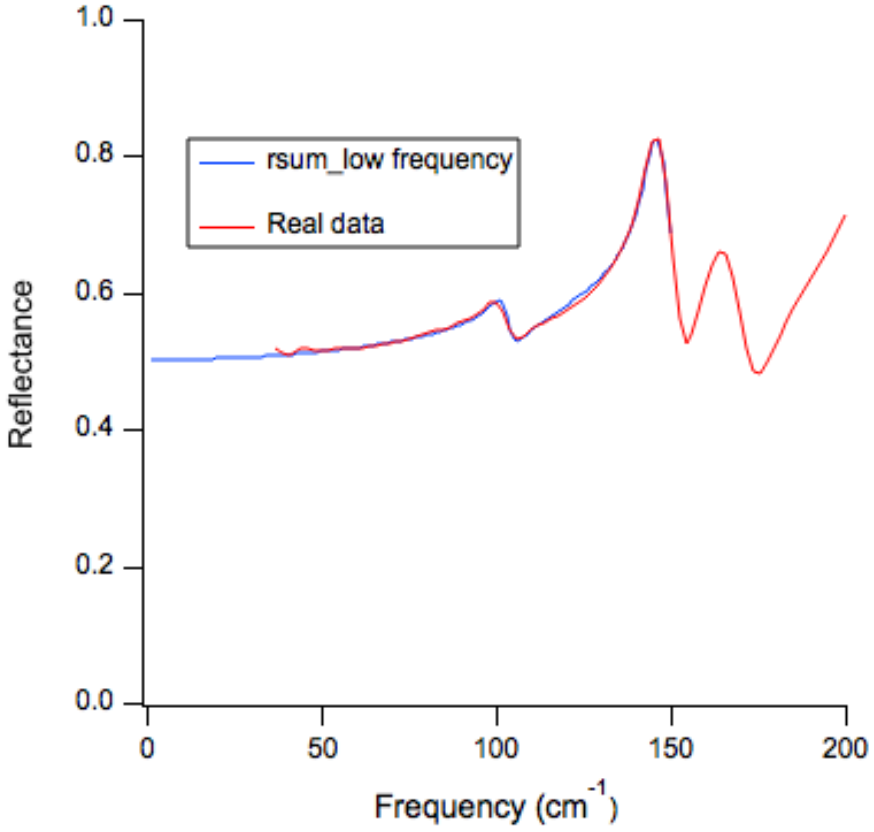

Figure 5.9: Sample low frequency extrapolation generated using the Lorentz model

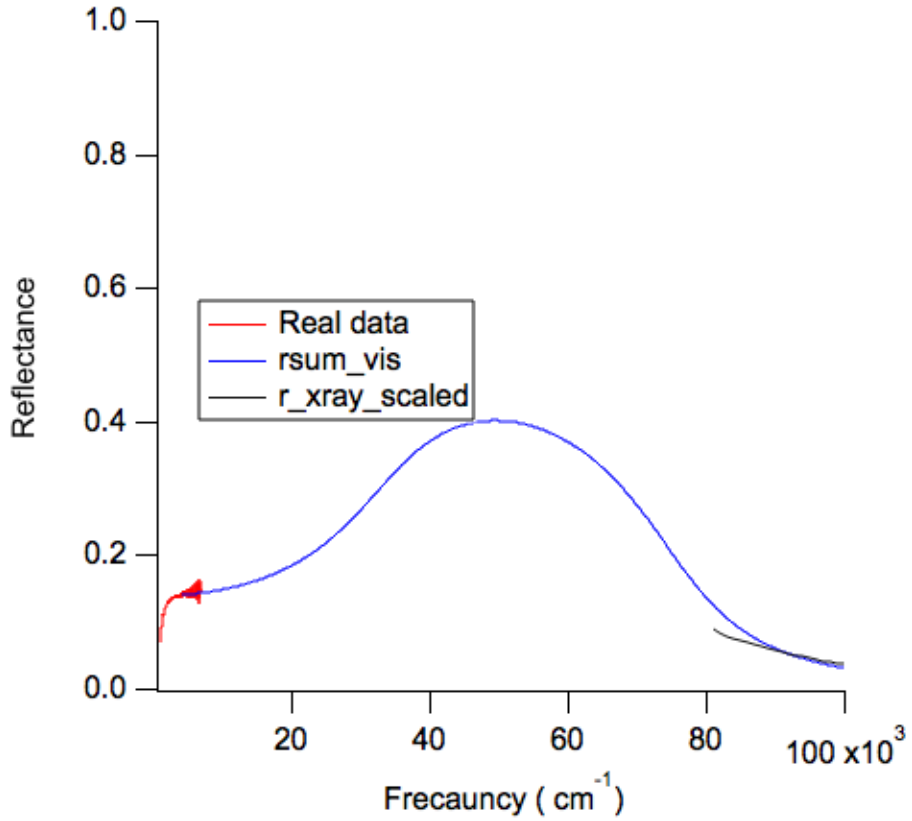

Figure 5.10: One oscillator model for reflectance between 7000 cm^{-1} 120000 cm^{-1}

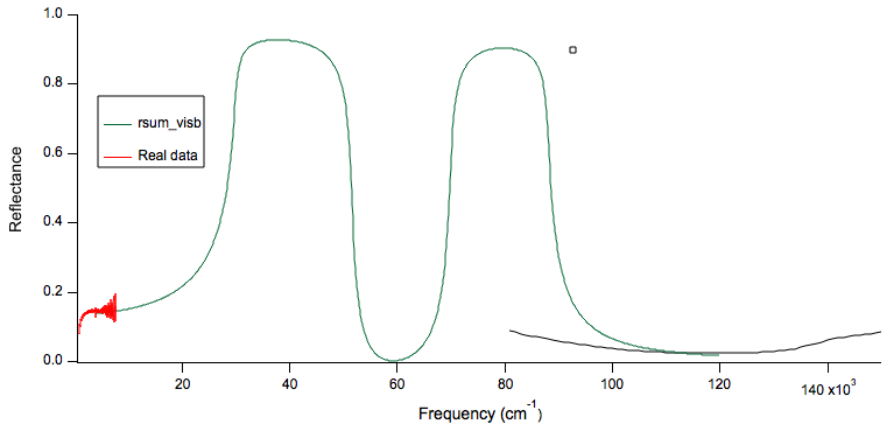

Figure 5.11: Two oscillator model for reflectance between 7000 cm^{-1} 120000 cm^{-1}

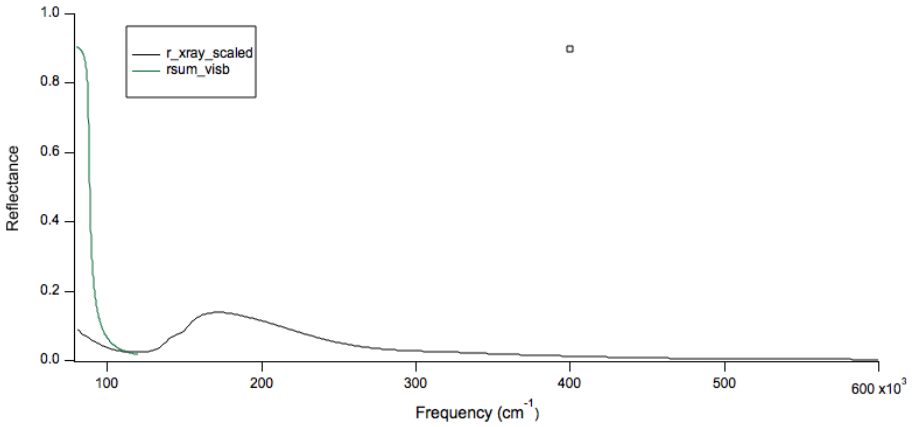

Figure 5.12: X-Ray reflectivity generated using Tanner's method[57]

note the effect of non-zero p and non-unity α by comparing the red curve and green curve.

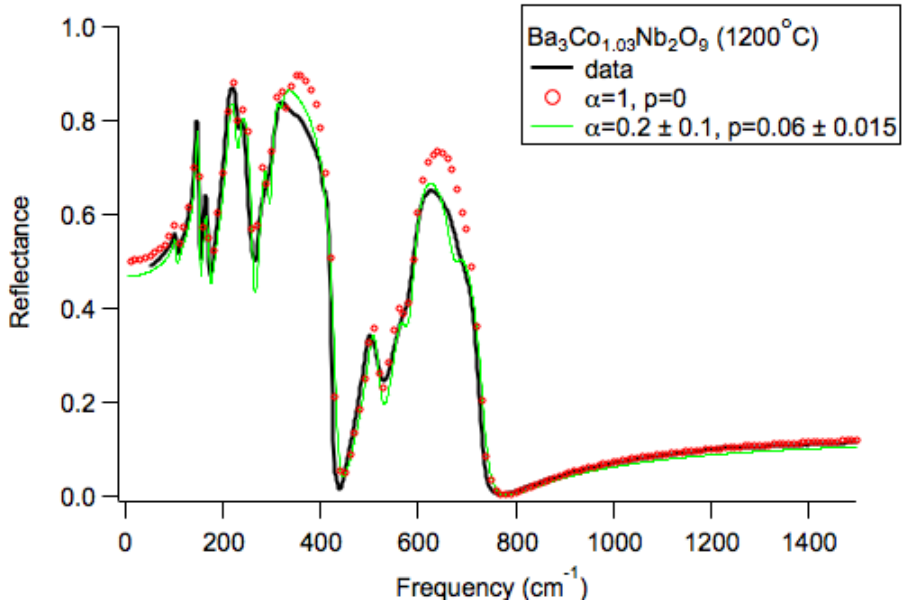

Figure 5.13: The effect of density using Lichtenecker model for $Ba_3Co_{1.03}Nb_2O_9$ sintered at temperature 1200 C°.

Figure 5.14 shows the KK conductivity of the samples of $Ba_3Co_{1.03}Nb_2O_9$ sintered at different temperature. Note that the highest absorption at frequency approximately 200 cm^{-1} (highest high dipole moment). The 200 cm^{-1} absorption increases with increasing sintering temperature (density).

Figure 5.15 shows the real part of k-k dielectric function of samples $Ba_3Nb_2Co_{1.03}O_9$ made at different sintering temperatures. As shown in the figure the sample with the highest density (sintered at 1425° C) has highest value of dielectric permittivity at 53 cm^{-1} around 38 compared with the sample that has lowest

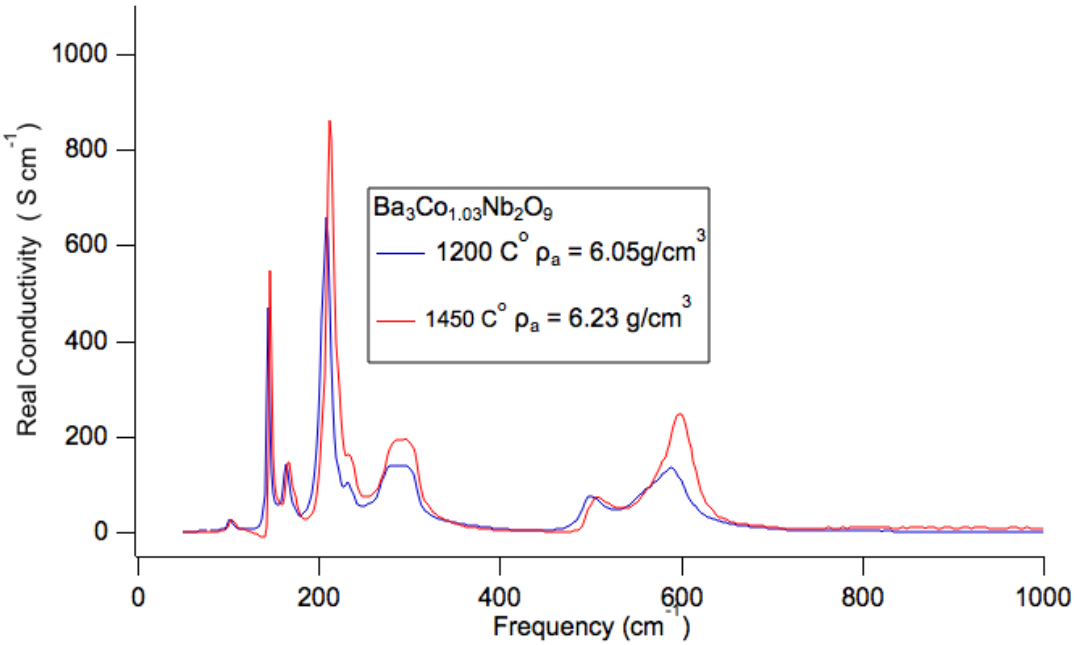

Figure 5.14: The optical conductivity versus frequency of $Ba_3Co_{1.03}Nb_2O_9$ samples made in different temperature

density (sintered at 1200C°) which has lowest permittivity value around 32 at $\omega = 50cm^{-1}$(the lowest frequency measured).

5.3.5 Effect of Cobalt concentration.

Fig 5.16 shows the reflectance of $Ba_3Co_{1.03}Nb_2O_9$ and $Ba_3Co_{0.93}Nb_2O_9$ samples of the same degree of ordering and approximately same density. The change of Cobalt concentration affects just two bands around 300 cm^{-1} and 600 cm^{-1}.

Fig 5.17 shows the K-K optical conductivity $Ba_3Co_{1.03}Nb_2O_9$ and $Ba_3Co_{0.93}Nb_2O_9$ samples of the same degree of ordering and approximately same density. Note that changing the concentration of cobalt does not have strong impact on the optical conductivity. Two peaks, one centered near 150 cm^{-1} and one near 600 cm^{-1} are affected.

Figure 5.18 shows the real part of dielectric function of samples of $Ba_3Co_{1.03}Nb_2O_9$ and $Ba_3Nb_2Co_{0.93}O_9$ with similar density and degree of order. There is a bigger effect in near 300 cm^{-1} than near 600 cm^{-1} in the ϵ_1 spectrum.

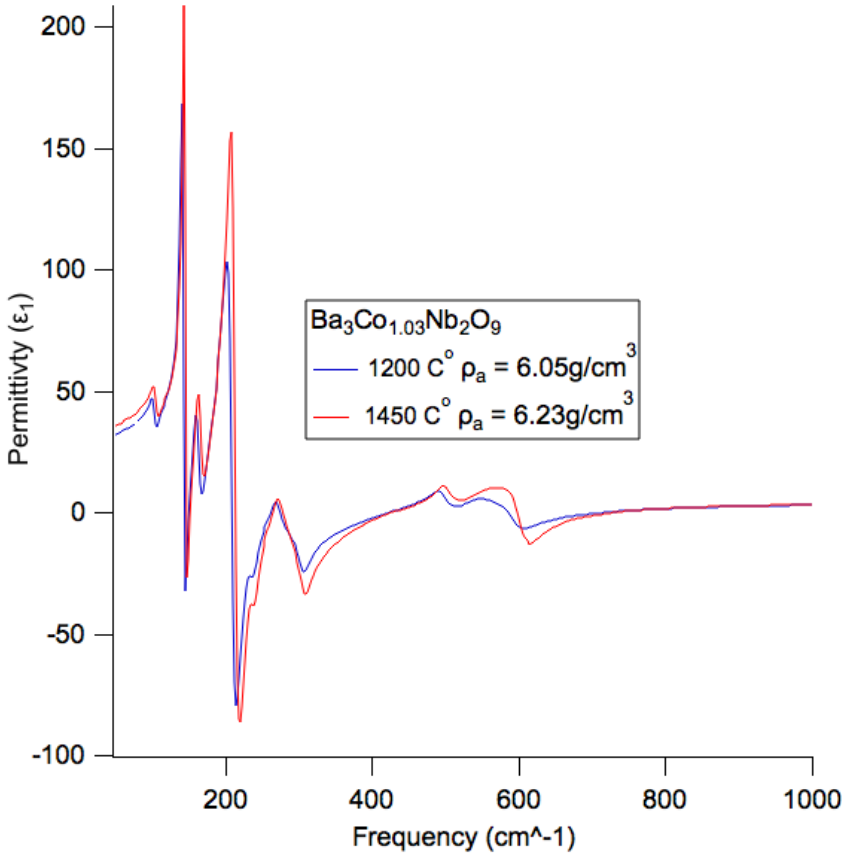

Figure 5.15: The real part of dielectric function versus frequency for $Ba_3Nb_2Co_{1.03}O_9$ samples made in different temperature

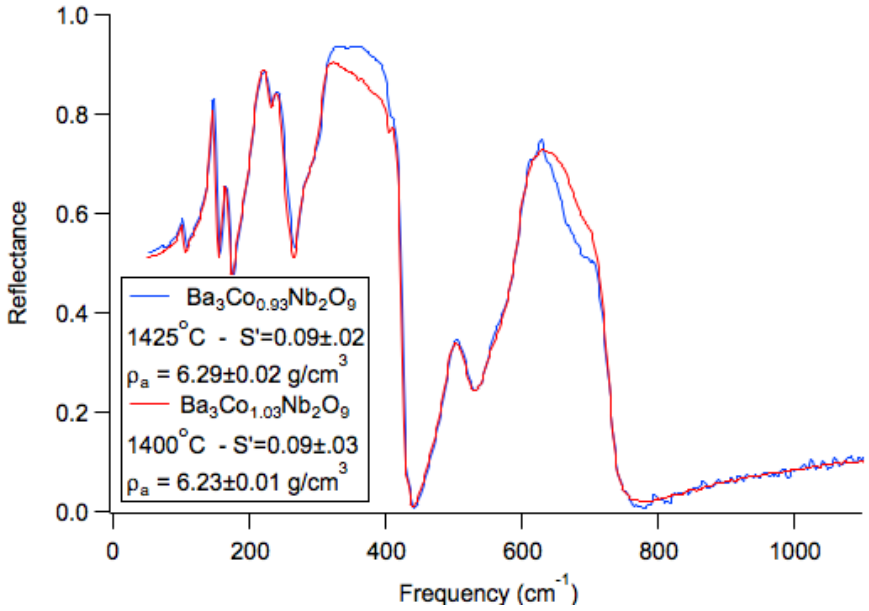

Figure 5.16: FIR reflectance of $Ba_3Co_{0.93}Nb_2O_9$ and $Ba_3Co_{1.03}Nb_2O_9$ samples have same density and degree of order, but different Cobalt concentration.

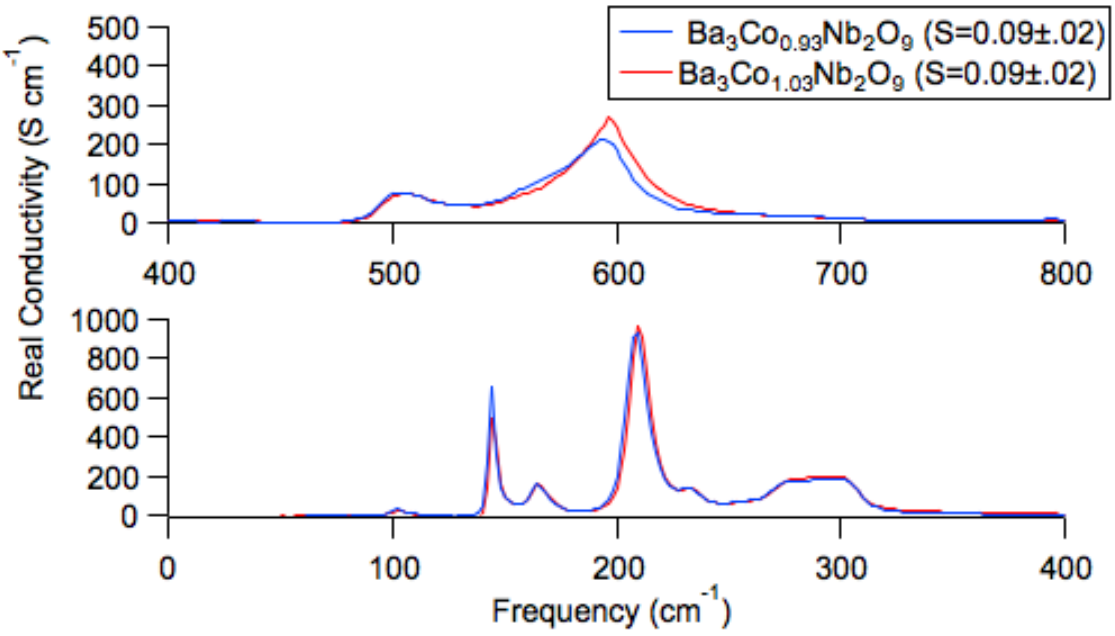

Figure 5.17: The optical conductivity versus frequency of $Ba_3Co_{0.93}Nb_2O_9$ and $Ba_3Co_{1.03}Nb_2O_9$ samples having different concentration of cobalt, but approximately the same degree of ordering [S′ = 0.09 ±0.02] and density [6.29 g/cm^3]

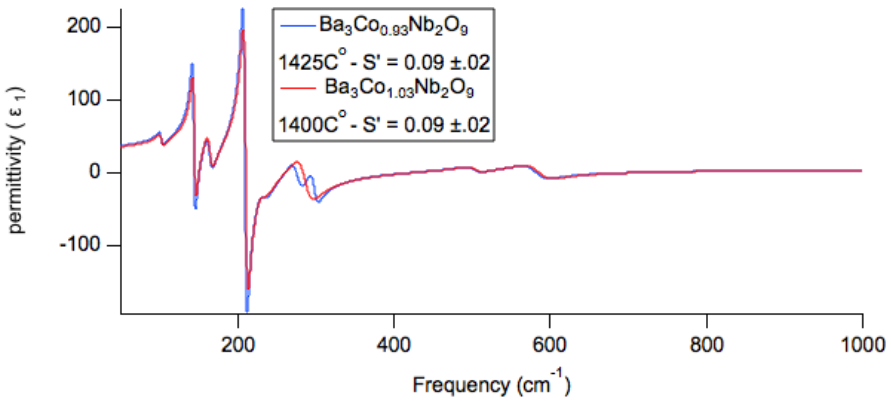

Figure 5.18: The real part of dielectric function versus frequency of $Ba_3Nb_2Co_{1.03}O_9$ and $Ba_3Nb_2Co_{0.93}O_9$ samples having different concentration of cobalt, but approximately the same degree of ordering [S′ = 0.09 ±0.02] and density [6.29 g/cm^3]

5.3.6 Effect of ordering

Fig 5.19 compares the reflectance of samples which have different degrees of ordering, but the same density. Note that the effect of ordering appear on all peaks.

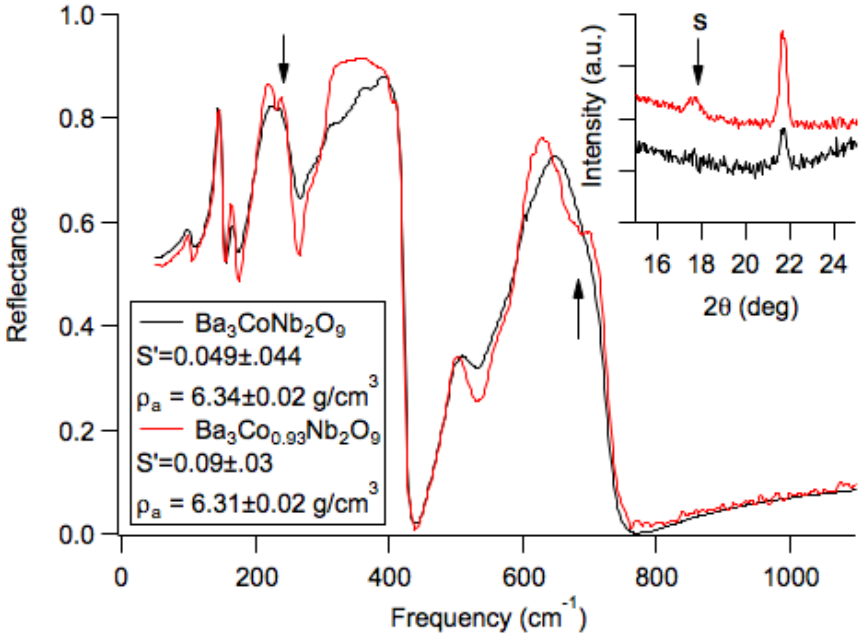

Figure 5.19: The effect of ordering on the reflectance e of $Ba_3CoNb_2O_9$ -O_2 and $Ba_3Co_{0.93}Nb_2O_9$ samples having same density but different ordering

Fig 5.20 shows the effect of order on the optical conductivity of samples with different degrees of ordering, but the same density. Note that the effect of ordering appears on all peaks. Note that the ordering has a big effect on the data. The sample with the lowest degree of ordering has much broader peaks than the samples with higher ordering indicating higher scattering and loss.

Fig 5.21 shows the effect of ordering on the permittivity of samples having different degrees of ordering, but the same density. Note that the effect of ordering appears on all peaks.

5.3.7 Effect of Barium Concentration

Fig 5.22 shows the effect of Barium concentration on the optical conductivity of $Ba_{2.97}CoNb_2O_9$ and $Ba_3Co_{0.93}Nb_2O_9$ samples that have the same density and degree of ordering, but different Barium concentration. Note the effect of

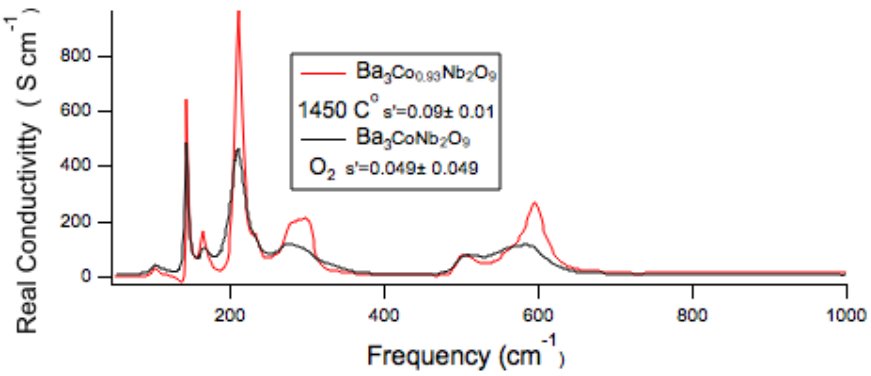

Figure 5.20: The effect of ordering on the real conductivity of samples having the same density but different ordering

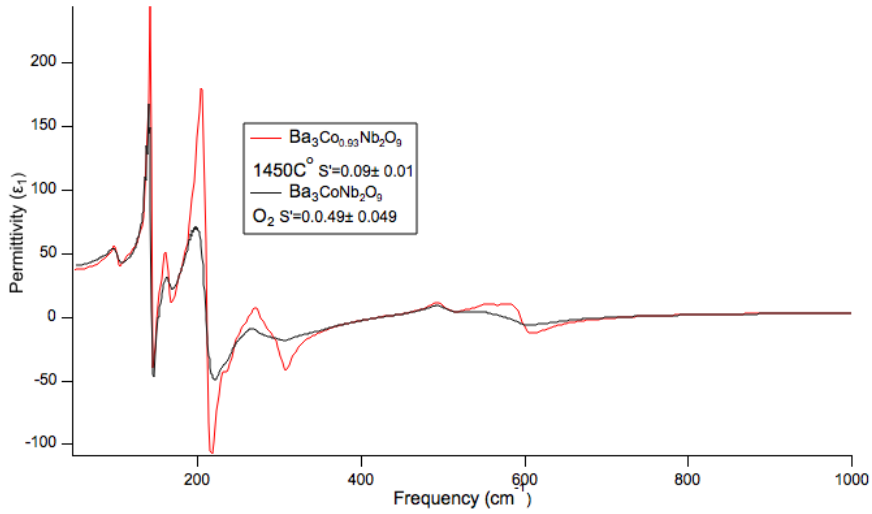

Figure 5.21: The effect of ordering on the dielectric permittivity of samples having the same density but different ordering

change of Barium concentration appears at three peaks near (220 cm^{-1}, 300 cm^{-1} and 600 cm^{-1})

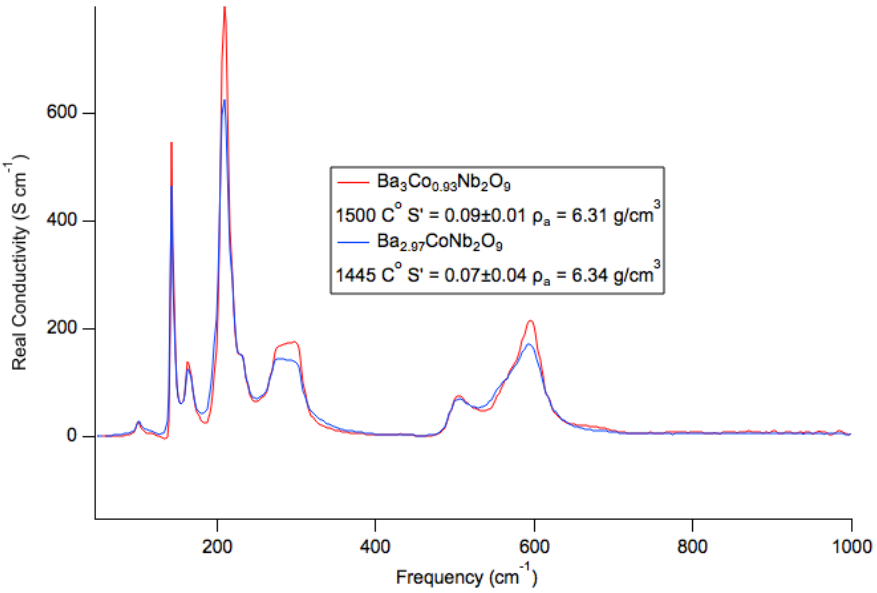

Figure 5.22: The effect of Barium concentration on optical conductivity

Fig 5.23 shows the effect of Barium concentration on the dielectric permittivity of $Ba_{2.97}CoNb_2O_9$ and $Ba_3Co_{0.93}Nb_2O_9$ samples which have the same density and degree of ordering, but different Barium concentration.

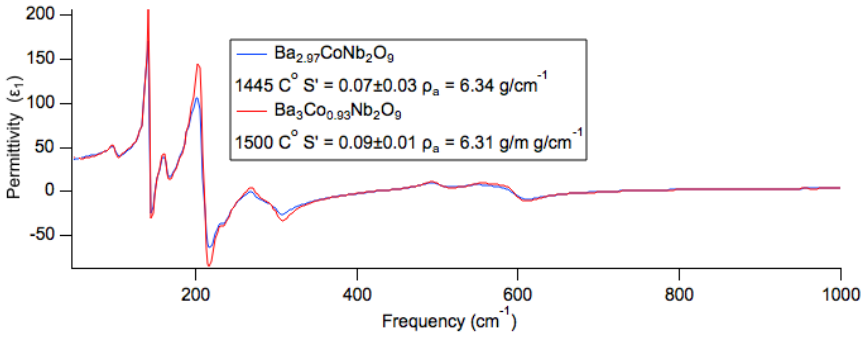

Figure 5.23: The effect off Barium concentration on dielectric permittivity

5.3.8 Microwave properties

Many previous workers have estimated microwave dielectric properties from infrared reflectance. An example appears in Fig 5.24.

Fig 5.25 shows the effect of density on the permittivity and dielectric loss in the microwave range for samples of $Ba_3Co_{1.03}Nb_2O_9$. The curve were generated

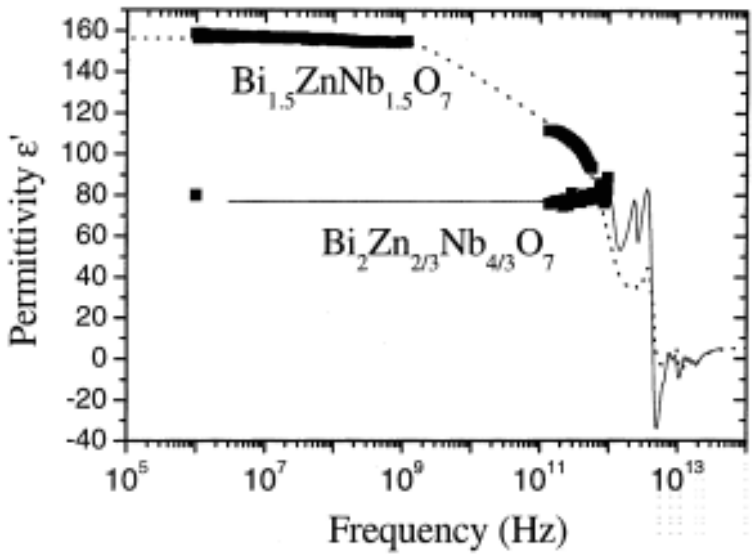

Figure 5.24: Example of using the Lorentz model to estimate the dielectric permittivity at microwave frequency (For frequency 10^6 Hz using capacitance method, for frequency between 10^6 Hz to $3\times$ 10^9 using co-axial reflection method and for frequency between 10^{10} Hz to 10^{12} Hz using transmission [58].

from the Lorentz oscillator fit to the reflectance data. As shown in the figure the highest value of ϵ_1, approximately 34.4, is for the sample has the highest density (sintered at 1425°C).

Fig 5.26 shows the effect of Cobalt concentration on the permittivity and dielectric loss in the microwave range for samples of $Ba_3Co_{1.03}Nb_2O_9$ and $Ba_3Co_{0.93}Nb_2O_9$ with the same density and degree of ordering. Both samples have approximately the same value of ϵ_1. The change in cobalt concentration does not have a strong impact on the dielectric function in microwave range.

Fig 5.27 shows the effect of ordering on the permittivity and dielectric loss in the microwave range for samples of $Ba_3CoNb_2O_9$ - O_2 and $Ba_3Co_{0.93}Nb_2O_9$ having different degrees of ordering , but the same density. Note that the different cobalt concentration does not have a strong impact on the dielectric function, for this reason we know that, this figure shows just the effect of ordering. As shown in the figure the sample with greatest disordering has higher value of ϵ_1, but also higher dielectric loss.

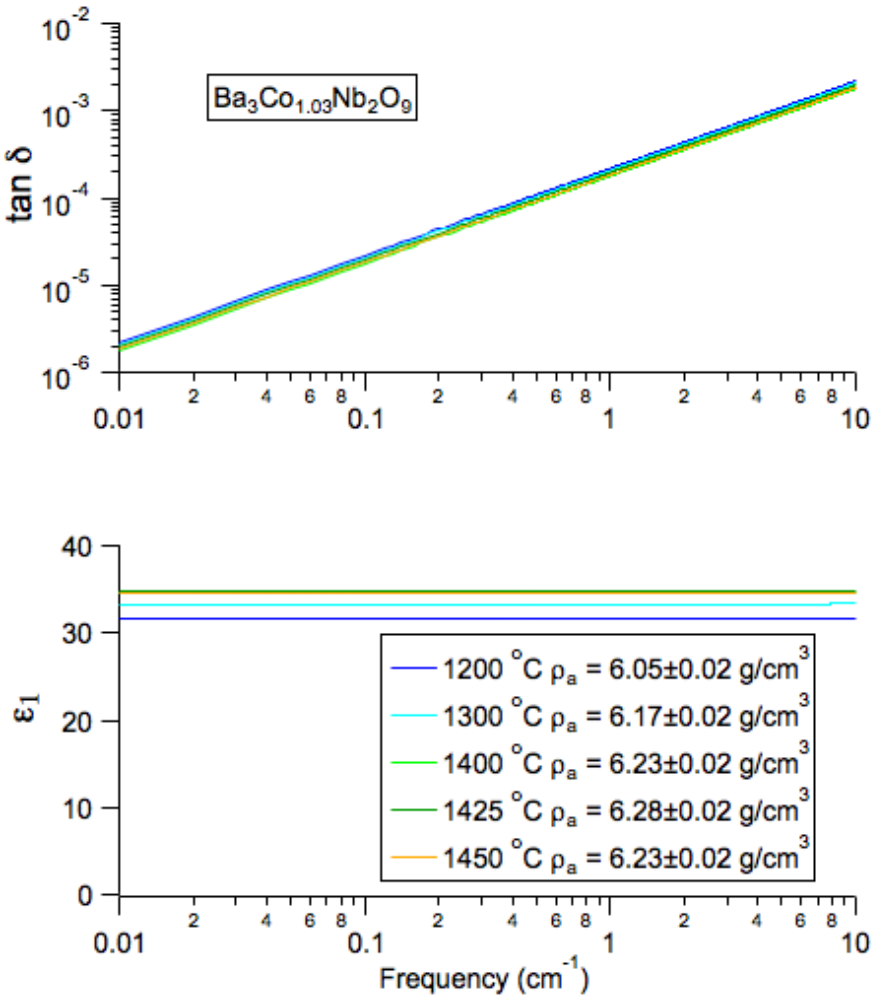

Figure 5.25: The estimated dielectric loss and ϵ_1 for samples having different density, extrapolated using the Lorentz model for the infrared reflectivity.

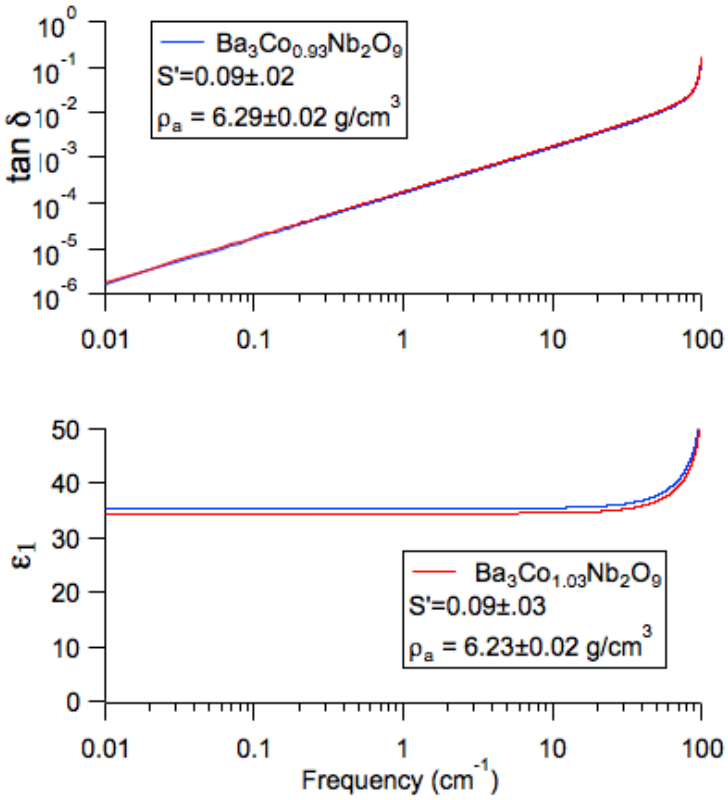

Figure 5.26: The real part of dielectric function and the dielectric loss versus frequency for $Ba_3Nb_2Co_{1.03}O_9$ and $Ba_3Nb_2Co_{0.93}O_9$, with approximately the same S′ and density at microwave frequencies . The curve were made by extrapolating the Lorentz oscillator model.

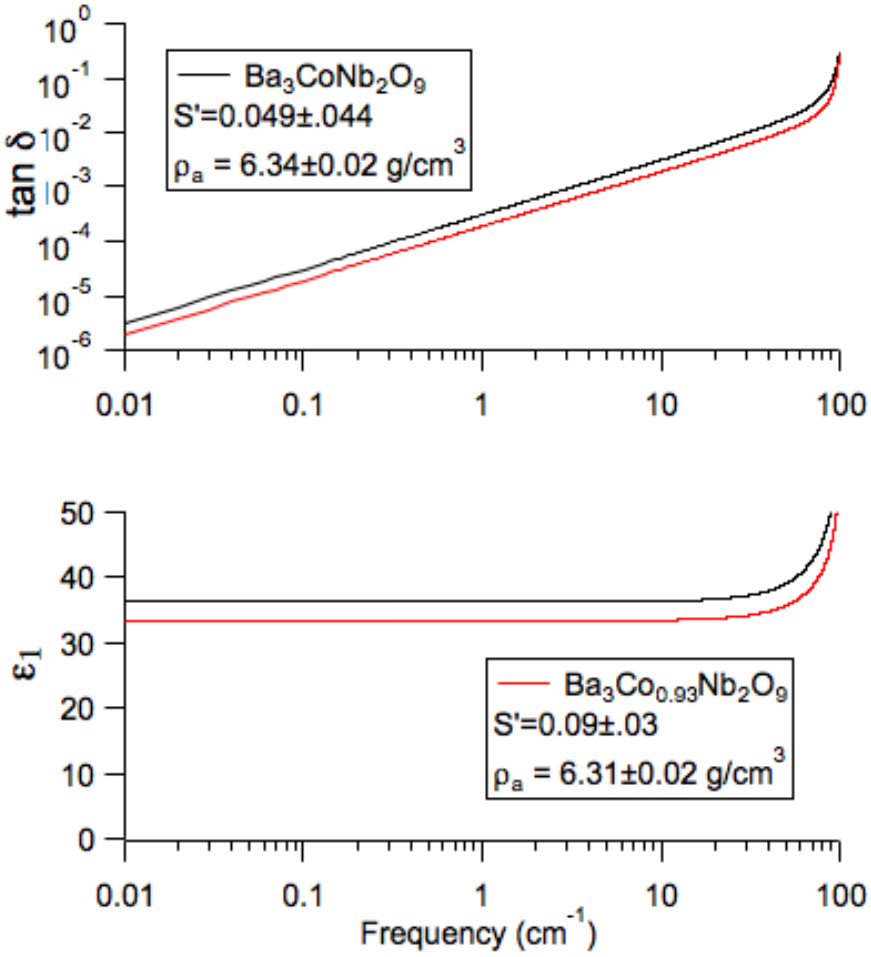

Figure 5.27: The effect of ordering of samples having the same density but different ordering at microwave frequencies. The extrapolation was made by using the Lorentz model

5.4 Comparison With Other Work

Previous workers have studied the effect of sintering temperature on the degree of ordering of BCN as is shown in Fig. 5.28[59]. Note that there is essentially no change in the small superlattice peak intensity with sintering temperature. Fig 5.2 shows the super peaks of $Ba_3Co_{1.03}Nb_2O_9$ samples sintered at different temperature where the superlattice peaks appear to decrease in size with sintering temperature. This is in contrast to research with the different compound ($BaMg_{1/3}Nb_{2/3}O_3$ [BMN]) which showed a strong relationship between sintering temperature and degree of ordering which increases sintering temperature is increasing the degree of ordering as shown in Fig 2.3.

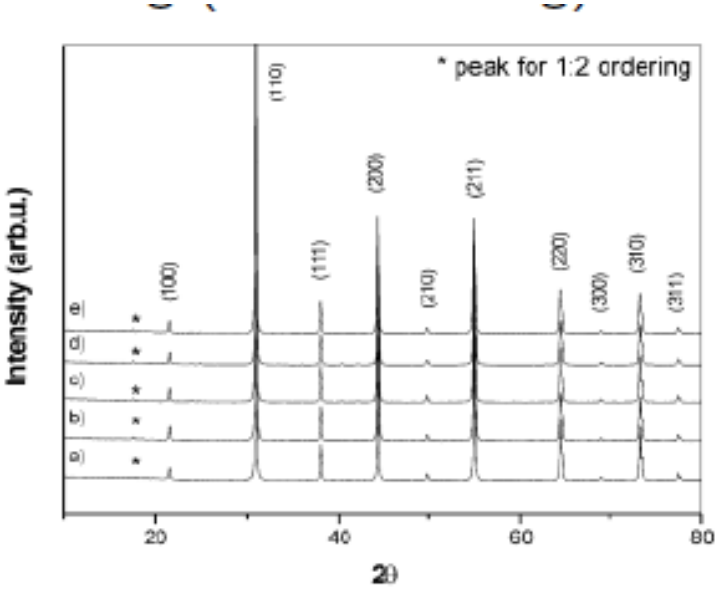

Figure 5.28: XRD patterns of BCN sample ceramic sintered at: (a) 1350°C, (b) 1400°C, (c) 1450°C, (d) 1480°C and (e) 1550°C for 6h.

The microwave Dielectric permittivity and Quality factor in this study are listed in table 5.3 where the values were found by extrapolation Lorentz oscillator model fit to the reflectance. This results agree with previous research which found dielectric permittivity around 32 to 34 using different methods as shown in table 5.4.

Note that the microwave Q×f values listed in table 5.3 which are found by the extrapolation Lorentz model are greater than those found using other method listed in table 5.4. This is suggesting that for BCN there are other loss mechanisms in BCN that should be studied with other techniques.

Sample Name	Sintering temperature (°C)	ϵ_1	Q× f
$Ba_3Co_{0.93}Nb_2O_9$	1400	31.8	140186.7
$Ba_3Co_{0.93}Nb_2O_9$	1425	36.1	420168
$Ba_3Co_{0.93}Nb_2O_9$	1450	35.9	162162.3
$Ba_3Co_{0.93}Nb_2O_9$	1500	34.4	142180.2
$Ba_3CoNb_2O_9$	1500	38.7	211267.5
$Ba_3Co_{1.03}Nb_2O_9$	1200	32.1	142857
$Ba_3Co_{1.03}Nb_2O_9$	1300	32.9	150000
$Ba_3Co_{1.03}Nb_2O_9$	1400	33.9	166666.8
$Ba_3Co_{1.03}Nb_2O_9$	1425	34.9	150754.5
$Ba_3Co_{1.03}Nb_2O_9$	1450	34.1	159574.5
$Ba_3CoNb_2O_9$ (O_2)	-	36.3	96774
$Ba_{2.97}CoNb_2O_9$	1445	34.1	130434.8

Table 5.3: The values of ϵ_1 and quality factor at wavenumber 0.1 cm^{-1} (3GHz) estimated from Lorentz model

Sample Name	ϵ_1	Q × f	Method	Ref
$Ba(Co_{1/3}Nb_{2/3})O_3$	32- 34	80000 - 85000 GHz (f= GHz)	Cavity reflection	59
(1-x) $Ba(Co_{1/3}Nb_{2/3})O_3$	34.5	97000 GHz	Dielectric resonator	60
$Ba_3Co_{1+?}Nb_2O_{9+y}$	30- 33	80000 - 90000 GHz (f= GHz)	Dielectric resonator	61
$Ba(Co_{1/3}Nb_{2/3})O_3$	32	66,500 GHz (f= 4GHz)	The parallel plate method	62

Table 5.4: The values of ϵ_1 and quality factor at wavenumber 0.1 cm^{-1} estimated from Lorentz model

This study also shows the strong effect of density on the optical properties, which has not been studied before in BCN.

Chapter 6

Conclusion

Studying the dielectric properties of ceramic samples of $Ba_{3+y}Co_{1+x}Nb_2O_9$ with different sintering temperatures between 1200 °C to 1500 °C has been done using x-ray and infrared reflectance spectroscopy. In this work three different parameters were studied: density , Cobalt and Barium concentration and B-site cation ordering.

The optical conductivity and dielectric permittivity were determined by using the KK analysis. Reflectance data fitting was done using two different models, the Lorentz oscillator model and the Lichtenecker's model.

Density measurements were done using two methods, the Geometric method and the Archimedes method. Both results are very close.

The density has the biggest impact on the optical properties (Dielectric permittivity and optical conductivity). Microwave permittivity increases with density and microwave loss decreases with ordering. On the other hand the Cobalt and Barium concentration do not have a big impact on the dielectric function except for the effect on ordering.

Dielectric permittivity values of $Ba_{3+y}Co_{1+x}Nb_2O_9$ estimated by using the Lorentz model are found to be between 34 to 36 in the microwave range.

Actual measurements of the dielectric function at microwave frequencies would be interesting to study further.

Bibliography

[1] Ghanshyam Pilania. *First Principles Studies of ABO3 Perovskite Surfaces and Nanostructures*. Ph.D. thesis, University of Connecticut, (2012).

[2] Joao Elias Figueiredo Soares Rodrigues, Debora Morais Bezerra, Adeilton Pereira Maciel and C. W. A. Paschoala, *Synthesis and structural ordering of nano-sized $Ba_3B'Nb_2O_9$ (B' = Ca and Zn) powders*. Preprint submitted to Materials Chemistry and Physics, (2013).

[3] S. Bindra Narang and Shalini Bahel *Low loss dielectric ceramics for microwave applications: a review* Journal of Ceramic processing Research .Vol. 11, No. 3, pp. 316 -321 (2010).

[4] Dmytro Grebennikov *Application of Positron Annihilation Spectroscopy to the Study of Defects in Perovskite Type Materials* . MSc thesis, McMaster University, (2007).

[5] Peter K. Davies and Jianzhu Tong *Effect of Ordering-Induced Domain Boundaries on Low-Loss $Ba(Zn_{1/3}Ta_{2/3})O_3$ - $BaZrO_3$ Perovskite Microwave Dielectrics*. Journal of the American Ceramic Society, Vol 80 [7], pages 1727-1740 (1997).

[6] Rachel Tarvin *A-Site and B-Site Order in $(Na_{1/2}La_{1/2})(Mg_{1/3}Nb_{2/3})O_3$ Perovskite*. Journal of the American Ceramic Society, Vol 87 [5], pages 859 -863, (2004).

[7] Kazuaki Endo, Kenji Fujimoto and Kyohei Murakawa *Dielectric Properties of Ceramics in $Ba(Co_{1/3}Nb_{2/3})O_3$-$Ba(Zn_{1/3}Nb_{2/3})O_3$ Sol id Solutionss*. J. Am. Ceram. SOC., 70 [9] C-215-C-218 (1987).

[8] Kanta and Dheeraj Kumar *Study the Perovskite-Type Mixed Metal Oxides with the General Formal ABO3*. International Journal of Research in Science And Technology, Vol. No. 3, pages 1-7, (2014).

[9] Long Youwen. *A-site ordered quadruple perovskite oxides* . Chinese Physics B, 25(7),(2016).

[10] Fancis S. Galasso *Structure, Properties and Preparation of Perovskite-Type Compounds*. International series of monographs in solid state physics, Vol 5, pages 1-12, (1969).

[11] Roberto L. Moreira and Franklin M. MatinagaAnderson Dias *Raman-spectroscopic evaluation of the long-range order in* Appl. Phys. Lett. 78, 428 (2001).

[12] Rachel Tarvin and Peter K. Davies *A-Site and B-Site Order in (Na1/2La1/2)(Mg1/3Nb2/3)O3 Perovskite* J. Am. Ceram. Soc., 87 [5] 859 - 863 (2004).

[13] S. Kawashima, M. Nishida, 1. Veda, and H. Ouchi. *Ba(Zn1/3Ta2/3)O3 Ceramics with Low Dielectric Loss at Microwave Frequencies* J. Am. Ceram. Soc., 66,421 (1983)

[14] Peter K. Davies and Jianzhu Tong *Effect of Ordering-Induced Domain Boundaries on Low-Loss* $Ba(Zn_{1/3}Ta_{2/3})O_3$ - $BaZrO_3$ *Perovskite Microwave Dielectrics*. Journal of the American Ceramic Society, Vol 80 [7], pages 1727-1740 (1997).

[15] A. Sawada and T. Kuwabara. *Infrared Study of Ba(Mg1/3Ta2/3)03 Ceramics for Microwave Resonators.* Ferroelectrics, 95:205, (1989).

[16] I.G. Siny, R. Tao, R.S. Katiyar, R. Guo, and A.S. Bhalla. *Raman Spectroscopy of Mg-Ta Order-Disorder in* $Ba(Mg_{1/3}Ta_{2/3})O_3$. J. Phys. Chem. Solids, 59:181, 1998.

[17] Dibyaranjan Rout. *Structure, Electrical and Raman Spectroscopy Studies of Lead Ytterbium Tantalate Based Ceramics*. Phd thesis, (2006).

[18] A.J. Jacobson, B.M. Collins, and B.E.F. Fender. *A Powder Neutron and X-ray Diffraction Determination of the Structure of Ba3Ta2Zn09: an Investigation of Perovskite phases in the System Ba-Ta-Zn-O and the Preparation of* $Ba_2TaCdO_{5.5}$ *and* $Ba_2CeInO_{5.5}$ Acta Cryst. B, 32:1083, (1976).

[19] A. Ioachim, M.I. Toacsan, L. Nedwlcu and L. Mihut *High-Q BZT Ceramics for Microwave Applications*. electroscience '08, Trondheim, Norway, (2008).

[20] Hideki Yoshioka *Ordering of Cations in* $Ba(Mg_{1/3}Nb_{2/3})O_3$ *and* $Ba(Zn_{1/3}Nb_{2/3})O_3$ The Chemical Society of Japan, 60,3433-3434(1987).

[21] K. M. Luk and K. W. Leung *Dielectric Resonator Antenna - Possible Candidate for Adaptive Antenna Arrays*. University of Mississippi, USA.

[22] Dipali Soren, Rowdra Ghatak, Rabindra K. Mishra, and Dipak R. Poddar. *Dielectric Resonator Antennas: Designs and Advances*. Progress In Electromagnetic's Research B, Vol. 60, 195 - 213, (2014).

[23] Taras Kolodiazhnyi, M.S. *Semiconducting and dielectric properties of Barium,Titanates, Tanttalates and Niobates with perovskite structure*. Phd Thesis, Mc Master University, (2002).

[24] V. Komarov, S. Wang and J. Tang. *Permittivity and Measurements.* Washington State University, pages 3696-3711. Encyclopedia of RF and Microwave Engineering, Edited by Kai Chang. (2005).

[25] Edward C. and Liang Ph.D *An Overview of High Q TE Mode Dielectric Resonators and Applications* . Microwave journal ,(2015).

[26] R. J. Collier and A. D. Skinner. *Microwave Measurements* 3rd Edition, IET Electrical Mesurment series 12, (2007).

[27] A.G. Belous and O.V. Ovchar *Mw Dielectrics with Perovskite-like Structure Based on Smcontaining Systems.* J. Europ. Ceram. Soc., 19:1119, (1999).

[28] J. J. Wu and X. M. Chen. *Modified* $Ba_{6-3x}N\ d_{8+2x}\ Ti_{18}\ O_{54}$ *microwave dielectric ceramics* J. Europ. Ceram. Soc., 19:1123, (1999).

[29] L-C. Tien, C-C. Chou, and D-S. Tsai. *Microstructure of $Ba(Mg_{1/3}Ta_{2/3})O_3$-$BaSnO_3$ microwave dielectrics.* Ceram. Intern., 26:57,(2000).

[30] Mailadil T. Sebastian. *Dielectric Materials for Wireless Communication.* Linacer House Jordan Hill, Oxford, (2008).

[31] W. Wersing. *Current Opinion in Solid State and Materials Science.* V[1], 715, (1996).

[32] Martin H. Weik *Fiber Optic Standard Dictionary* . Springer Science + Business Medias B.V, Vol 11, (1997).

[33] A. Templeton, X. Wang, S. J. Penn, S. J. Webb, L.F. Cohen, and N. Alford. *Microwave Dielectric Loss of Titanium Oxide.* J.Am. Ceram. So., 83, 95 (2000).

[34] M.A. Akbas and P.K. Davies. *Domain Growth in $Pb(Mg_{1/3}Ta_{2/3})O_3$ Perovskite Relaxor Ferroelectric Oxides.* J. Am. Ceram. Soc., 80:2933, (1997).

[35] H. Matsumoto, H. Tamura, and K. Wakino. *$Ba(Mg,Ta)O_3$-$BaSnO_3$ high-Q dielectric resonator.* Jpn. J. Appl. Phys., 30:2347, (1991).

[36] S. Kawashima, N. Nishada, 1. Veda, and H. Ouchi. *$Ba(Zn_{1/3}T_{2/3})O_3$ Ceramics with Low Dielectric Loss at Microwave Frequencies.* J. Am. Ceram. Soc., 66:421, (1983).

[37] L. Nedelcu, C. Busuioc, M. G. Banciu, R. Ramer. *$Ba(X_{1/3}Ta_{2/3})O_3$ Complex Perovskites for Microwave and Millmeter-Wave Application* Scientific Research, project number PN-II-RU-PD-2011-3-0237 and Core Program PN09-45.

[38] Frederick Wooten *Optical Properties of Solid* New York: Academic, (1972).

[39] M. Fox *Optical Properties of Solid* New York: Oxford University Press, (2001).

[40] David J Griffiths. *Introduction to Electrodynamics* Prentice Hall Upper Saddle River, New Jersey 07458, (1999).

[41] *https://commons.wikimedia.org/wiki/File:Fresnel.JPG*

[42] *http://www.tcm.phy.cam.ac.uk*

[43] I. F. Almog, M. S. Bradley, and V. Bulovi. *The Lorentz Oscillator and its Applications* Electromagnetic Energy: From Motors to Lasers (2011).

[44] Eugene Hecht *Optics* chapter3, Addison- Wesley, (2011).

[45] V. Lucarini, J.J. Saarinen, K.E. Peiponen and E.M. Vartiainen *Kramers-Kronig Relations in Optical Materials Research*. Joensuu, Camerino, Toronto, and Lappeenranta, (2004).

[46] Olga Krivokhvost *Conventional and Nonconventional Kramers-Kronig Analysis in Optical Spectroscopy*. Master's Thesis,Lappeenranta University of Technology, (2014).

[47] D. Nuzhnyy, J. Petezlt, I. Rychetsky, and G. Trefalt *Effective Dielectric Function of Porous* $Pb(Mg_{1/3}Nb_{2/3})O_3$ *Ceramics*. Phys. Rev. B. 89,214307 (2014).

[48] Tarik Zakri, Jean-Paul Laurent and Michel Vauclin *Theoretical Evidence for Lichtenecker's Mixture Formulae' Based on the Effective Medium Theory*. J. Phys. D: Appl. Phys. 31,pages 1589 - 1594, (1998).

[49] Dmytro Grebennikov *Influence of Nonstoichiometry in Ba3BNb20 9 on Microwave Properties*. PhD Thesis, XX - 174, McMaster University (2011).

[50] *Ihttps://nanohub.org/resources/4111/download/2008.02.20-mse640-l4.pdf*.

[51] *http://skuld.bmsc.washington.edu/ merritt/bc530/bragg/*.

[52] *Powder Diffraction Optics for Smart Lab X-ray diffractmeter* The Rigaku Journal, 26(20), (2010).

[53] *http://chemistry-reference.com/density/*.

[54] *http://hyperphysics.phy-astr.gsu.edu/hbase/pbuoy2.html*

[55] *https://en.wikipedia.org/wiki/Toluene*

[56] $http://felix.physics.sunysb.edu/\ allen/252/PHY251_Michelson.html$

[57] D. B. Tanner *Use of x-ray Scattering Functions in Kramers-Kronig Analysis of Reflectance* Physical Review B 91, 035123 (2015)

[58] J. Petzelt, S. Kamba *Submillimetre and Infrared Response of Microwave Materials: Extrapolation to Microwave Properties* Materials Chemistry and Physics 79, 175 - 180, (2003).

[59] A. G. Belousa, O. V. Ovchara, A. V. Kramarenkoa, Bostjan Jancarb, Jana Bezjakb, and Danilo Suvorovb *Low-Loss Microwave Ceramics Based on Non-Stoichiometric Perovskites* $Ba(Co_{1/3}Nb_{2/3})O_3$ *and* $Ba(Zn_{1/3}Nb_{2/3})O_3$ Ferroelectrics, 367:149 - 162, (2008).

[60] C. Woo, Sahn Nahm, S. Yoon, H Min and H. Lee. *Microstructure and Microwave Dielectric Properties of (1- x)*$Ba(Co_{1/3}Nb_{2/3})O_3$ *-* $xBa(Zn_{1/3}Nb_{2/3})O_3$ *Ceramics* Jpn. J. Appl. Phys. pp. 6964 - 6968. Vol. 42 (2003).

[61] A. G. Belousa, O. V. Ovchara, A. V. Kramarenkoa, Bostjan Jancarb, Jana Bezjakb, and Danilo Suvorovb *Effect of Nonstoichiometry on the Structure and Microwave Dielectric Properties of* $Ba(Co_{1/3}Nb_{2/3})O_3$ Inorganic Materials, Vol. 46, No. 5, pp. 529-533, (2010).

[62] F. Azough, C. Leach, R. Freer. *Effect of nonstoichiometry on the structure and microwave dielectric properties of* $Ba(Co_{1/3}Nb_{2/3})O_3$ *ceramics* Journal of the European Ceramic Society 26 ,pp. 2877 - 2884, (2006) .

Parameters Obtained in Lorentz Oscillator Model Fits to Reflectance

Appendix A

Parameters Obtained in Lorentz Oscillator Model Fits to Reflectance

Oscillator number	ω_0	Γ	ω_P
1	103±1	7± 3	103 ±15
2	144.5±0.3	4.7± 0.5	339± 7
3	164.8± 0.4	10 ± 1	258 ± 9
4	210.9 ±0.4	9± 1	679 ± 12
5	232 ± 1	20 ± 3	299 ±29
6	279 ± 1	25 ± 2	456± 25
7	300.3± 0.7	18± 2	394± 23
8	378 ± 2	29 ± 5	83 ± 8
9	503.6 ± 0.6	24 ± 2	3299 ± 8
10	562± 2	37 ± 5	378± 28
11	593.6 ± 0.6	28± 1	508± 17
12	669 ± 1	58 ± 2	190 ± 7

Table A.1: The Drude-Lorentz model parameters of $Ba_3Co_{0.93}Nb_2O_9$ sintered at temperature 1400° C ($\epsilon_\infty = 4.7$)

Oscillator number	ω_0	Γ	ω_P
1	102± 1	86± 2	108 ±11
2	144.3±0.1	4.5± 0.3	363± 5
3	164.45± 0.2	9.7 ± 0.6	284 ± 7
4	209.1 ±0.3	10± 1	729 ± 8
5	232 ± 1	18 ± 3	262 ±26
6	278.9 ± 0.51	28 ± 2	499± 13
7	299.6± 0.4	13± 1	299± 20
8	302±0	8±0	262± 0
9	502.3 ± 0.5	28 ± 2	335 ± 7
10	562± 1	47 ± 3	468± 25
11	590.3 ± 0.5	26± 2	399 ± 23
12	673 ± 1	62 ± 5	153 ± 9

Table A.2: The Drude-Lorentz model parameters of $Ba_3Co_{0.93}Nb_2O_9$ sintered at temperature 1425°C ($\epsilon_\infty = 5.2$)

Oscillator number	ω_0	Γ	ω_P
1	102± 1	86± 4	107 ±30
2	144.7±0.5	4.4± 0.8	356± 10
3	165± 1	10 ± 2	294 ± 20
4	211 ±1	8± 1	753 ± 20
5	235 ± 2	15 ± 4	278 ± 40
6	278 ± 1	16 ± 2	447± 20
7	300± 1	14± 2	411± 20
8	302±0	8±0	262± 0
9	503 ± 1	25 ± 3	333 ± 10
10	557± 1	27 ± 5	349± 30
11	591 ± 1	30 ± 2	552 ± 20
12	686 ± 7	40 ± 20	54 ± 20

Table A.3: The Drude-Lorentz model parameters of $Ba_3Co_{0.93}Nb_2O_9$ sintered at temperature1450°C ($\epsilon_\infty = 5.2$)

Oscillator number	ω_0	Γ	ω_P
1	102± 1	86± 4	102±30
2	145.1±0.5	4.8± 0.8	345± 10
3	165± 1	11 ± 2	279 ± 20
4	212±1	10± 1	706 ± 20
5	233 ± 2	15 ± 4	369 ± 40
6	280 ± 1	17 ± 2	464± 20
7	301± 1	12± 2	388± 20
8	302±0	8±0	262± 0
9	504 ± 1	26 ± 3	339 ± 10
10	560± 1	33 ± 5	399± 30
11	592 ± 1	28 ± 2	481 ± 20
12	675± 7	36 ± 20	108± 20

Table A.4: The Drude-Lorentz model parameters of $Ba_3Co_{0.93}Nb_2O_9$ sintered at temperature 1500° C ($\epsilon_\infty = 5.04$)

Oscillator number	ω_0	Γ	ω_P
1	103±1	5± 3	88 ±18
2	144.6±0.3	4.7± 0.6	339± 7
3	164.8± 0.4	10 ± 1	258 ± 9
4	210.9 ±0.4	9± 1	679 ± 12
5	232 ± 1	20 ± 3	299 ±29
6	279 ± 1	25 ± 2	456± 25
7	300.3± 0.7	18± 2	394± 23
8	378 ± 2	29 ± 5	83 ± 8
9	503.6 ± 0.6	24 ± 2	3299 ± 8
10	562± 2	37 ± 5	378± 28
11	593.6 ± 0.6	28± 1	508± 17
12	669 ± 1	58 ± 2	190 ± 7

Table A.5: The Drude-Lorentz model parameters of $Ba_3Co_{1.03}Nb_2O_9$ sintered at temperature 1200°C ($\epsilon_\infty = 5.1$)

Oscillator number	ω_0	Γ	ω_P
1	102±1	7± 4	99±21
2	144.9±0.4	5.2± 0.7	321± 10
3	165.1± 0.5	10 ± 1	278 ± 13
4	210.5 ±0.5	8± 1	702 ± 14
5	233 ± 2	18 ± 4	289 ±34
6	279 ± 1	23 ± 2	467± 26
7	299.3± 0.7	15± 2	390± 26
8	302±0	8±0	262± 0
9	503.4 ± 0.8	24 ± 2	314 ± 11
10	560± 2	35 ± 7	366± 42
11	591 ±1	31± 2	514± 26
12	679 ± 3	39± 10	73 ± 11

Table A.6: The Drude-Lorentz model parameters of $Ba_3Co_{1.03}Nb_2O_9$ sintered at temperature 1300°C ° ($\epsilon_\infty = 4.9$)

Oscillator number	ω_0	Γ	ω_P
1	103±1	5± 4	96±21
2	145.1±0.4	4.6± 0.7	337± 10
3	165.1± 0.5	9± 1	280 ± 13
4	211.1 ±0.8	7± 1	715 ± 14
5	233 ± 2	19 ± 4	307 ±34
6	278 ± 1	21 ± 2	465± 26
7	299.1± 0.7	14± 2	414± 26
8	302±0	8±0	262± 0
9	504.5 ± 0.8	22 ± 2	312 ± 11
10	558± 2	35 ± 7	338± 42
11	592 ±1	32± 2	572± 26
12	679 ± 3	34± 10	74 ± 11

Table A.7: The Drude-Lorentz model parameters of $Ba_3Co_{1.03}Nb_2O_9$ sintered at temperature 1400° C ($\epsilon_\infty = 5.2$)

Oscillator number	ω_0	Γ	ω_P
1	102±1	8± 4	131±22
2	144.8±0.4	4.6± 0.7	356± 11
3	164.5± 0.5	10± 1	301 ± 14
4	210.0 ±0.5	7± 1	726 ± 15
5	233 ± 2	19 ± 5	272 ±41
6	274 ± 1	18 ± 3	383± 36
7	288.8± 0.9	11± 4	305± 59
8	302± 1	12± 2	317± 31
9	503 ± 1	23 ± 2	323 ± 11
10	556± 2	34 ± 6	369± 31
11	590 ±1	31± 2	503± 18
12	684 ±1	24± 9	49 ± 9

Table A.8: The Drude-Lorentz model parameters of $Ba_3Co_{1.03}Nb_2O_9$ sintered at temperature 1425° C ($\epsilon_\infty = 4.9$)

Oscillator number	ω_0	Γ	ω_P
1	105±2	7± 5	108±26
2	146.8±0.5	4.6± 0.8	344± 13
3	167.3± 0.7	10± 21	283 ± 17
4	213.2±0.6	7± 1	711 ± 19
5	236 ± 2	19 ± 4	344 ±40
6	279 ± 1	19 ± 2	447± 27
7	300.5± 0.7	14± 2	410± 28
8	329± 2	12± 5	1307± 25
9	507 ± 1	23 ± 3	321 ± 14
10	561± 2	33 ± 6	388± 37
11	595 ±1	29± 2	532± 21
12	689 ±6	27± 14	46 ±12

Table A.9: The Drude-Lorentz model parameters of $Ba_3Co_{1.03}Nb_2O_9$ sintered at temperature 1450° C ($\epsilon_\infty = 5.2$)

Oscillator number	ω_0	Γ	ω_P
1	103± 1	11± 8	148 ±22
2	144.1±0.4	5.3± 0.7	378± 10
3	167± 1	14± 3	257 ± 19
4	214 ±1	16± 1	818 ± 8
5	233 ± 0	15 ± 0	264 ± 0
6	274 ± 1	22 ± 2	414± 17
7	201± 1	16± 2	323± 18
8	333± 1	19 ± 2	209 ± 12
9	508 ±1	25 ± 2	338 ± 13
10	554± 1	33± 5	392± 28
11	590± 1	40± 1	483 ± 17
12	674.6 ± 1	36 ± 5	-

Table A.10: The Drude-Lorentz model parameters of $Ba_3CoNb_2O_9$ O_2 ($\epsilon_\infty = 4.9$)

Oscillator number	ω_0	Γ	ω_P
1	103± 1	6± 3	115 ±20
2	144.1±0.3	3.6± 0.5	403± 9
3	164.7± 0.4	10± 1	326 ± 11
4	208.5 ±0.4	3± 1	781 ± 9
5	234 ± 1	15 ± 3	264± 23
6	272 ± 1	16 ± 1	390± 15
7	288.8± 0.4	8± 2	283± 22
8	301.8± 0.5	8± 1	262 ± 16
9	503 ±1	22 ± 2	342 ± 8
10	557± 1	30± 3	403± 21
11	589± 1	29± 1	469 ± 15
12	683 ± 3	36 ± 8	60± 8

Table A.11: The Drude-Lorentz model parameters of $Ba_3CoNb_2O_9$ sintered at temperature 1500° C ($\epsilon_\infty = 5.03$)

Oscillator number	ω_0	Γ	ω_P
1	103± 1	8± 3	117 ±20
2	144.7±0.2	5.2± 0.5	348± 10
3	165± 1	11± 1	270 ± 11
4	211.3 ±0.4	9± 1	707 ± 9
5	234 ± 1	18 ± 3	347± 23
6	276 ± 1	20 ± 1	428± 15
7	300± 1	16± 2	286± 22
2 8	331.3± 0.5	17± 1	152 ± 16
9	505 ±1	23 ± 2	311 ± 8
10	557± 1	32± 3	386± 21
11	593± 1	33± 1	521 ± 15
12	689 ± 3	17 ± 8	31± 8

Table A.12: The Drude-Lorentz model parameters of $Ba_{2.97}CoNb_2O_9$ sintered at temperature 1445° C ($\epsilon_\infty = 5.02$)